HHS Public Access

Author manuscript

Cell Rep. Author manuscript; available in PMC 2022 October 29.

Published in final edited form as:

Cell Rep. 2022 September 27; 40(13): 111431. doi:10.1016/j.celrep.2022.111431.

Nanoscopic dopamine transporter distribution and conformation are inversely regulated by excitatory drive and D2 autoreceptor activity

Matthew D. Lycas[1], **Aske L. Ejdrup**[1], **Andreas T. Sørensen**[1], **Nicolai O. Haahr**[1], **Søren H. Jørgensen**[1], **Daryl A. Guthrie**[2], **Jonatan F. Støier**[1], **Christian Werner**[3], **Amy Hauck Newman**[2], **Markus Sauer**[3], **Freja Herborg**[1], **Ulrik Gether**[1,4,*]

[1]Molecular Neuropharmacology and Genetics Laboratory, Department of Neuroscience, Faculty of Health and Medical Sciences, University of Copenhagen, Maersk Tower 7.5, 2200 Copenhagen, Denmark

[2]Medicinal Chemistry Section, Molecular Targets and Medications Discovery Branch, National Institute on Drug Abuse-Intramural Research Program, National Institutes of Health, Baltimore, MD 21224, USA

[3]Department of Biotechnology and Biophysics, Biocenter, Julius-Maximilians-Universität Würzburg, Am Hubland, 97074 Würzburg, Germany

[4]Lead contact

SUMMARY

The nanoscopic organization and regulation of individual molecular components in presynaptic varicosities of neurons releasing modulatory volume neurotransmitters like dopamine (DA) remain largely elusive. Here we show, by application of several super-resolution microscopy techniques to cultured neurons and mouse striatal slices, that the DA transporter (DAT), a key protein in varicosities of dopaminergic neurons, exists in the membrane in dynamic equilibrium between an inward-facing nanodomain-localized and outward-facing unclustered configuration. The balance between these configurations is inversely regulated by excitatory drive and DA D2 autoreceptor activation in a manner dependent on Ca^{2+} influx via N-type voltage-gated Ca^{2+} channels. The DAT nanodomains contain tens of transporters molecules and overlap with nanodomains of PIP2 (phosphatidylinositol-4,5-bisphosphate) but show little overlap with D2 autoreceptor, syntaxin-1,

*Correspondence: gether@sund.ku.dk.

AUTHOR CONTRIBUTIONS

M.D.L. performed all experiments and wrote the analyses not mentioned hereafter. A.L.E. devised the cluster size algorithm, identified mRNA expression data, and performed D2 receptor histology. A.T.S. performed electrophysiology and generated the construct encoding Cre recombinase under control of a truncated TH promotor. N.O.H. performed the D421N CAD cell experiments. S.H.J. cloned Kir2.1 and mNaChBac plasmids and made noncommercially available viruses. D.A.G. and A.H.N. invented and synthesized the fluorescent cocaine analogs. J.F.S. optimized the DA neuron culture protocol. M.D.L., F.H., and U.G. conceptualized the study, designed the research, and interpreted data. U.G., F.H., M.S., and C.W. supervised the research. M.D.L., U.G., and F.H. wrote the paper with contributions from M.S. and all other authors.

DECLARATION OF INTERESTS

The authors declare no competing interests.

SUPPLEMENTAL INFORMATION

Supplemental information can be found online at https://doi.org/10.1016/j.celrep.2022.111431.

and clathrin nanodomains. The data reveal a mechanism for rapid alterations of nanoscopic DAT distribution and show a striking link of this to the conformational state of the transporter.

In brief

Lycas et al. use super-resolution microscopy to investigate nanoscale regulation of the dopamine transporter (DAT) in the membrane of presynaptic release sites. The results show conformation-dependent localization of DAT to PIP2-enriched nanodomains and that this localization is inversely regulated by excitatory input and dopamine D2 autoreceptor activity in a Ca^{2+}-dependent manner.

Graphical Abstract

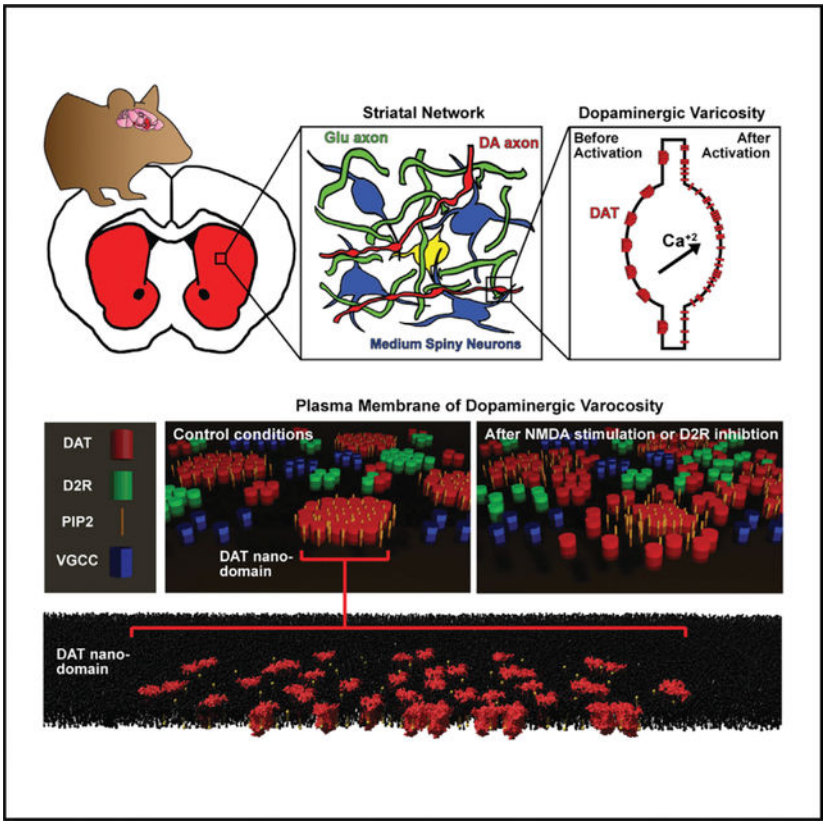

INTRODUCTION

In its 15 years of utilization, super-resolution microscopy has improved our insights into the molecular organization and dynamic regulation of pre- and postsynaptic structures in the brain. It has become clear that regulatory processes of fundamental importance for spatial and temporal control of synaptic signaling occur at a nanoscale level. In excitatory synapses, for example, it is now believed that α-amino-3-hydroxy-5-methyl-4-isoxazolepropionic acid (AMPA)- and N-methyl D-aspartate (NMDA)-type ionotropic glutamate receptors segregate into distinct nanodomains in the postsynaptic density and that this co-organization plays a critical role in synaptic physiology (Choquet and Hosy, 2020; Groc and Choquet, 2020).

Such studies highlight the importance of observing past the diffraction limit of visible light while still leveraging the labeling strategies and live imaging compatibility that light microscopy provide (Choquet and Hosy, 2020; Groc and Choquet, 2020; Liu and Kaeser, 2019).

Much less is known about the nanoscale architecture of the presynaptic compartment in neurons releasing modulatory transmitters like dopamine (DA). DA neurons project from the midbrain to the basal ganglia, the limbic system, and the prefrontal cortex to mediate the role of DA in motor functions, reward mechanisms, and learning processes (Bjorklund and Dunnett, 2007; Iversen, 1975; Tritsch and Sabatini, 2012). DA neurons have remarkable axonal arbors with numerous release sites (i.e., varicosities) (Descarries et al., 1996; Giguere et al., 2019), and DA neurotransmission differs from classical fast synaptic transmission by operating perhaps primarily via “volume transmission”; that is, DA is predominantly released from non-synaptic release sites to act on target cells often located micrometers away (Borroto-Escuela et al., 2018; Descarries et al., 1996). It remains elusive how the different molecular components in the dopaminergic release sites need to be organized at a nanoscale level and regulated individually to enable proper neurotransmitter release and reuptake.

A key regulator of DA neurotransmission, the DA transporter (DAT), is highly expressed in the varicosities of DA neurons and removes released DA from the extracellular space. DAT has received attention as the primary target for therapeutic agents, such as methylphenidate, and drugs of abuse, such as methamphetamine and cocaine (German et al., 2015; Kristensen et al., 2011; Torres and Amara, 2007). DAT is subject to tight regulation through several mechanisms involving post-translational modifications, protein-protein interactions, and protein-lipid interactions (Bermingham and Blakely, 2016; Eriksen et al., 2010; German et al., 2015; Kristensen et al., 2011; Ramamoorthy et al., 2011; Torres, 2006). We have shown, by application of super-resolution imaging, that DAT regulation might involve mechanisms that cannot be revealed by more classic methods (Rahbek-Clemmensen et al., 2017). Our data showed that DAT localizes to discrete nanodomains in the plasma membrane of cultured DA neurons and that activation of NMDA receptors reduces DAT nanodomain localization (Rahbek-Clemmensen et al., 2017). Although this indicates that nanoscale dynamics in DA varicosities could be critical for controlling DA neurotransmission, the mechanisms and functional implications remain unknown.

Here we use several super-resolution imaging techniques and data analysis tools to investigate how DAT and associated molecular components at DA varicosities are dynamically regulated. Our results demonstrate that excitatory drive and D2 autoreceptor activity inversely regulate the conformational state of DAT and its localization in DA varicosities in a Ca^{2+}-dependent manner. The DAT nanodomains are phosphatidylinositol-4,5-bisphosphate (PIP2)-enriched nanodomains and separate from syntaxin-1 (STX-1), D2 autoreceptor, or clathrin nanodomains. In summary, the study uncovers a nanoscale regulation mechanism of an essential membrane protein in a modulatory transmitter terminal.

RESULTS

DAT shows nanodomain distribution in cultured neurons and striatal slices

There are a variety of strategies to resolve biological structures past the diffraction limit of light, but each method is associated with strengths, compromises, and potential artifacts. True nanoscopic organizational principles should therefore be observed across a variety of super-resolution methods and model systems. Our previous direct stochastic optical reconstruction microscopy (dSTORM) work suggested that DAT distributes into nanodomains at DA varicosities of cultured midbrain DA neurons (Rahbek-Clemmensen et al., 2017). To substantiate this finding, we decided to assess DAT distribution across a variety of super-resolution methods and ultimately investigate whether DAT is distributed into nanodomains in intact tissue. First, by magneto-transfection, we expressed, in DA neurons, DAT with the photoconvertible fluorescent protein mEOS2 (Baker et al., 2010) fused to the N terminus. This enabled us to visualize distribution of the transporter by photo-activated localization microscopy (PALM) without use of antibodies. Images of tyrosine hydroxylase (TH)-positive varicosities revealed a clustered distribution of the mEos2 DAT signal surrounding the cytosolic TH signal (Figures 1A–1D), similar to that seen by imaging the endogenous DAT by dSTORM (Rahbek-Clemmensen et al., 2017). We next employed astigmatic 3D dSTORM to show that the DAT nanodomains were localized to the periphery of the varicosities, substantiating that DAT is found mainly in the plasma membrane (Figures 1E–1H). To assess the distribution of DAT in intact tissue, we analyzed coronal mouse brain slices (Figures 1I–1L). Wide-field imaging exposed the DAT-positive varicosities, and by dSTORM we could visualize DAT in single varicosities, showing a nanodomain distribution like that seen in cultured neurons (Figures 1I–1L). To exclude that the observed distribution of DAT was not caused by artifacts introduced by the single-molecule localization microscopy approach (e.g., “over-counting”; Shivanandan et al., 2014), we turned to expansion microscopy (ExM), where nanoscale spatial resolution is obtained by expanding the tissue sample using a polymer system (Chen et al., 2015; Truckenbrodt et al., 2019; Figures 1M–1P). Our images visualized the intermingled axonal network of DA neurons while observing clustering of DAT into nanodomains in varicosities (Figures 1M–1P). Summarized, the distribution of DAT into nanodomains in the plasma membrane of DA neurons was substantiated by several high-resolution imaging techniques.

In our subsequent studies, we decided to focus on the dSTORM technology because of its quantitative nature and single-molecule sensitivity. To derive quantitative measures for the clustered distribution of DAT, we employed the DBSCAN algorithm (density-based spatial clustering of applications with noise) (Ester et al., 1996; Rahbek-Clemmensen et al., 2017) and extracted two key parameters from the analysis: the size of the nanoclusters and the density of localizations within the clusters (Figures 1Q–1S). The size was quantified as the fraction of clusters with a diameter greater than 75 nm (Figure 1R). This size was chosen as a threshold to exclude any clusters that might be the result of amplified labeling of single proteins and, thus, might arise from the antibody labeling methodology. By assessing the density of localizations as well, we could determine changes in the number of molecules in a cluster without a change in cluster size. Dense clusters were defined as clusters with more than 80 localizations within a radius of 50 nm (dense clusters in red, Figure 1S). In

selected cases, we also employed Voronoi tessellation to compare the density distributions of localizations after pharmacological treatment in a parameter-free fashion (Levet et al., 2019). With this use of Voronoi tessellation, clusters themselves were not identified, but localization density changes could be detected with greater sensitivity (Figure 1T).

To estimate how many DAT molecules are present in an average DAT nanodomain defined by the DBSCAN analysis, we labeled cultured DA neurons with sequential dilutions of the primary DAT antibody (Ehmann et al., 2014; Siddig et al., 2020). This enabled us to define that a minimum cluster is made from approximately three localizations and that an average large cluster contains approximately 33 copies of the antibody, corresponding to 50–100 DAT molecules as a rough estimate (Figure S1). The same data series lent itself perfectly to cluster analysis by varied label density cluster verification, enabling us to distinguish between random clustering arising from multiple observations of single fluorophores and true clustering (Baumgart et al., 2016). Indeed, our analysis supported that DAT clustering reflects true nanodomain formation (Figure S2).

Nanodomain-localized DAT is preferentially in an inward-facing conformation

To assess the functional implications of DAT nanodomains, we investigated whether this could involve a conformational bias. Cocaine and cocaine-like inhibitors are known to bind with higher affinity to DAT in the outward-facing conformation than in the inward-facing conformation (Beuming et al., 2008; Loland et al., 2008; Newman et al., 2019). We envisioned, accordingly (and in line with Lebowitz et al., 2019), that an indirect measure of the conformational state of DAT inside and outside of the nanodomains could be obtained by parallel imaging of binding to DAT of a fluorescently tagged cocaine analog and of DAT itself; that is, as a result of its conformational bias, the cocaine analog would be expected to bind more to outward-facing than to inward-facing transporters at a subsaturating concentration. We labeled cultured DA neurons and mEos2-DAT-expressing CAD cells with DG3–63 (10 nM), an analog of cocaine tagged with JF_{646} suited for dSTORM (Figures 2A–2D). The DG3–63 signal generally appeared somewhat less clustered compared with that observed by our other approaches (Figure 1). This indicates preferential binding of DG3–63 to unclustered DAT, which was supported by dual-color images of DG3–63-labeled DAT and mEos2-DAT, showing a more dispersed DG3–63 signal compared with a more clustered mEOS2-DAT signal (Figures 2E–2G). The DG3–63 signal was specific because it was essentially eliminated by excess of unlabeled cocaine (Figure 2H). To quantify whether DG3–63 preferentially bound to unclustered DAT, we used a modification of the principles outlined by the colocalization extension of the Voronoi tessellation algorithm (Levet et al., 2019), where associated DG3–63 was identified by including DG3–63 localizations within 25 nm of an mEos2-DAT localization (Figures 2I–2K). The total mEos2-DAT Voronoi tessellated area distribution showed a preference for smaller tessellated areas, consistent with a clustered distribution (Figure 2L). In contrast, the mEOS2-DAT-associated DG3–63 localizations resided on larger Voronoi tessellated areas; hence, DG3–63 binding was not enriched in the DAT nanodomains containing the highest density of DAT molecules (Figure 2L). This suggests that nanoclustered DATs are less prone to bind DG3–63, consistent with a more inward-facing transporter conformation or a less accessible binding site. By analyzing the distribution of mEOS2-DAT after treatment with an excess and, therefore, saturating

concentration of cocaine, we observed dispersal of the signal. This supports the theory that forcing the transporter into an outward-facing conformation releases the transporter from the nanodomains (Figure S3A).

To further address this question, we examined the effect of the DAT inhibitors nomifensine, JHW007, and ibogaine on DAT nanoclustering in CAD cells expressing wild-type (WT) DAT. We used dSTORM and, thus, immunolabeling rather than mEOS2-DAT to make the data more compatible with our analyses on neurons and brain slices. Nomifensine is a cocaine-like inhibitor prone to self-administration (Spyraki and Fibiger, 1981) and, thus, prone to stabilize an outward-facing conformation (Beuming et al., 2008; Loland et al., 2008; Newman et al., 2019). JHW007 and ibogaine, however, are known to promote an inward-facing conformation of the transporter (Beuming et al., 2008; Kasture et al., 2016; Loland et al., 2008; Newman et al., 2019). A Voronoi tessellation analysis of the data showed that, although nomifensine decreased nanoclustering, JHW007 and ibogaine increased DAT clustering, consistent with the notion that an inward-facing conformation promotes nanodomain localization (Figures S3B and S3C).

We further rationalized that, if the nanoscale DAT distribution reflects its molecular conformation, then a redistribution would be expected for a DAT variant with a conformational bias. Accordingly, we compared, in transfected CAD cells, clustering of WT DAT with that of a disease-associated DAT mutation (D421N) shifted toward an inward-facing conformation (Hansen et al., 2014; Herborg et al., 2018; Figures 2M–2R). In agreement with our prediction, the data revealed, for D421N, a higher fraction of large clusters (diameter, >75 nm) and a higher fraction of localizations in dense clusters (Figures 2N, 2O, 2Q, and 2R) without a change in total number of detected localizations (Figure 2P). Collectively, the data support that DAT preferentially assumes an inward-facing conformation in DAT nanodomains, whereas the conformation outside of the nanodomains conceivably is more outward facing.

NMDA receptor activation declusters DAT in striatal slices

We next assessed whether DAT nanodomain distribution was sensitive to NMDA stimulation in intact tissue (Figures 2I–2P), as we observed previously in cultured neurons (Rahbek-Clemmensen et al., 2017). NMDA receptors are present in DA terminals, where they can stimulate DA release (Salamone et al., 2014). Acute coronal striatal slices were treated for 5 min with vehicle, NMDA, or NMDA plus the NMDA receptor antagonist (2R)-amino-5-phosphonovaleric acid (AP5) before DAT immunolabeling and dSTORM (Figure 3A). Because each dSTORM image contained a vast number of DAT-positive varicosities, we developed a collection algorithm for automated and unbiased isolation of these varicosities, allowing subsequent quantification of DAT clustering (Figures 3B and 3C). After NMDA treatment, the fraction of clusters greater than 75 nm and the faction of localizations in dense clusters decreased, an effect that was muted by the NMDA antagonist AP5 (Figures 3D and 3E). The comparisons were normalized to the control sample from the individual imaging session to correct for unavoidable variability in sample preparation and between imaging sessions. The data were supported by Voronoi tessellation showing that NMDA, but not NMDA plus AP5, reduced the fraction of smaller tessellated areas and, thus, clustering

(Figure 3F). We conclude that local activation of NMDA receptors in intact tissue promotes dispersal of DAT nanodomains.

DAT nanodomain localization is regulated by neuronal activity

We speculated whether persistent changes in membrane potential and, therefore, in neuronal excitability would affect DAT nanodomain distribution. To test this, we expressed the bacterial sodium channel (mNaChBac) or the inward rectifier potassium channel (Kir2.1) (Lin et al., 2010; Xue et al., 2014) in cultured DA neurons to make them more or less excitable, respectively (Lin et al., 2010). As a control, we also expressed an inactive mutant of mNaChBac (mNaChBac MUT) (Lin et al., 2010; Xue et al., 2014). In agreement with selective expression in DA neurons, we confirmed that transduced cells were also DAT positive (Figure S4). Electrophysiological recordings on single neurons showed that the pacemaker firing activity of DA neurons (Rayport et al., 1992) was enhanced in mNaChBac-expressing neurons and reduced in Kir2.1-expressing neurons with no significant change in mNaChBac MUT-expressing neurons (Figure S4). Analysis by dSTORM of DAT distribution in mNaChBac-expressing neurons showed decreased clustering, whereas for Kir2.1-expressing neurons, we saw a trend toward an increased fraction of large clusters and a significant increase in localizations within large dense clusters (Figures 4A–4D). No significant effect was seen for mNaChBac MUT (Figures 4C and 4D). Thus, DAT nanodomain localization in cultured DA neurons is regulated by persistent changes in excitability or firing activity, with increased activity leading to dispersal of DAT from nanodomains and decreased activity leading to increased nanodomain localization.

DAT nanodomain localization is regulated by Ca^{2+}

Because of the effect of neuronal excitability, we decided to investigate putative involvement of Ca^{2+} influx via voltage-gated Ca^{2+} channels (VGCCs) in NMDA-induced DAT declustering. Note that P/Q-type and N-type VGCCs should be present in DA terminals (Turner et al., 1993). While we observed no effect of blocking P/Q-type VGCCs with ω-agatoxin, the dispersing effect of NMDA on DAT clustering was essentially abolished by the N-type VGCC blocker ω-conotoxin (Figures 4E–4J; Videos S1 and S2). We next wanted to determine whether Ca^{2+} would be important per se by preincubating the neurons with the cell-permeable Ca^{2+} chelator BAPTA-AM ((1,2-Bis(2-aminophenoxy) ethane-N,N,N′,N′-tetraacetic acid tetrakis(acetoxymethyl ester)). BAPTA-AM blunted the response to NMDA (Figures 4K and 4L). The pharmacological data fit well with available single-cell mRNA sequencing data on DA neurons, supporting highest transcription of N-type VGCCs in DA neurons (Figure 4M; see STAR Methods for databases used). Taken together, NMDA-induced dispersal of DAT nanodomains appears to occur via a Ca^{2+}-dependent mechanism involving the activity of N-type VGCCs.

DAT nanodomain localization is regulated by the D2 autoreceptor

D2 autoreceptors in DA neurons act as negative feedback regulators, decreasing neuronal excitability and firing activity by opening of inhibitory G-protein-activated, inwardly rectifying potassium channels (Beckstead et al., 2004; Kuzhikandathil et al., 1998). We surmised that D2 autoreceptor activity might regulate localization of DAT to nanodomains and tested this by determining the effect of the D2 receptor antagonist haloperidol and

the D2 receptor agonist quinpirole. Incubation with 10 nM haloperidol for 5 min resulted in dispersal of DAT nanodomains with a reduced fraction of clusters greater than 75 m, fewer localizations in dense clusters, and a reduced fraction of smaller Voronoi tessellated areas (Figures 5A–5F; Videos S1 and S3). This effect is likely the result of haloperidol blocking the effect on D2 autoreceptors of DA released in the culture because of DA neuronal pacemaker activity (Figure S4). Consistent with this notion, co-incubation with an excess of quinpirole blocked the effect of haloperidol (Figures 5A–5F). We also observed that the effect of haloperidol was accompanied by an increase in cytoplasmic free Ca^{2+}, in agreement with D2 autoreceptor activity suppressing neuronal firing (Figures S5A and S5B). This prompted us to test whether the effect of haloperidol, like the effect of NMDA, was dependent on Ca^{2+} influx via N-type VGCCs. This appeared to be the case because ω-conotoxin, but not ω-agatoxin, eliminated the effect of haloperidol (Figures 5A–5F). Summarized, the data support that D2 autoreceptors are preoccupied with DA in neuronal culture and that the activity of these receptors can regulate DAT nanodomain localization via a Ca^{2+}-dependent mechanism.

To substantiate a correlation between D2 autoreceptor signaling, neuronal activity, and DAT nanoclustering, we incubated cultured DA neurons with an antibody directed toward the luminal end of the presynaptic vesicular protein synaptotagmin-1. Upon exocytotic release, this luminal epitope is exposed to the extracellular space; thus, the degree of synaptotagmin-1 labeling can be considered a proxy for exocytotic release activity (Truckenbrodt et al., 2018). Indeed, blocking the D2 autoreceptor with haloperidol caused dispersal of DAT nanoclusters accompanied by increased synaptotagmin-1 labeling, likely as a result of increased exocytotic release activity (Figure S5C). It is unlikely that the presumed increase in exocytotic release of DA directly regulates DAT and leads to dispersal of DAT nanodomains. Adding exogenous DA to the culture had no effect on DAT nanoclustering (Figure S3D), and DAT nanoclustering was unaffected by noribogaine, whereas nomifensine caused significant declustering of DAT (Figure S3D). This suggests that the transporter is already preoccupied by DA and, therefore, is active/cycling, which, as expected, pushes a fraction of the transporter molecules into an inward-facing nanoclustered configuration. In this scenario, no effect is expected of noribogaine as well as the data are consistent with the declustering seen in response to nomifensine that will compete DA away from the transporter.

Single-particle tracking supports nanodomain dispersal in response to neuronal activity

To obtain a better understanding of the dynamics underlying DAT nanodomain localization, we employed single-particle tracking (SPT)-dSTORM (Manley et al., 2008) to assess whether dispersal of DAT from nanodomains is accompanied by increased lateral mobility of DAT in the membrane. To allow visualization in live cells, we labeled DAT in DA neurons with a Janelia Fluor 549-conjugated cocaine analog, DG3–80, suited for live dSTORM (Guthrie et al., 2020; Figures 5G and 5H). Individual DAT tracks were captured with lengths of up to 1.6 s (100 frames, 16-ms frame rate), with the majority being 10–20 frames (Figures 5I and 5J). Separating tracks into those reflecting confined movements and those reflecting freely moving particles showed that ~90% of the tracks described freely moving particles (Figures 5K and 5L). This distribution (with most of the labeled molecules being

freely moving) likely reflects preferential binding of DG3–80 to unclustered DAT in the outward-facing conformation (Figure 2). The mean jump distance (i.e., the distance an individual molecule/particle has traveled between each image) was ~110 nm for all recorded tracks and ~50 nm for static tracks only (Figures 5M and 5N). Among the freely moving particles, there were even some that moved very fast with a mean jump distance of 200–350 nm (Figures 5M–5O). Both NMDA receptor activation and blockade of the D2 autoreceptors with either haloperidol or the neutral antagonist UH-232 increased the population of DAT molecules with mean jump distances of greater than 200 nm, indicative of a link between dispersal of DAT nanodomains and increased lateral mobility. The similar effects of UH-232 and haloperidol strongly suggest that their effects reflect blockade of D2 autoreceptors activated by DA, which is released because of DA neuronal pacemaker activity, and not inhibition of constitutive receptor activity (Strange, 2008).

DAT nanodomains overlap with PIP2 nanodomains

A key question is how the nanoscale distribution of DAT relates to other molecular components of DA terminals. We first turned to the plasma membrane phospholipid PIP2 (phosphatidylinositol 4,5-bisphosphate), which can bind DAT and, in doing so, modulate DAT activity (Belovich et al., 2019). Dual-color dSTORM on PIP2 and DAT in DA neurons showed, as expected (van den Bogaart et al., 2011), a distribution of the PIP2 signal into nanodomains (Figure 6). These nanodomains showed a remarkable overlap with DAT nanodomains, with the Voronoi tessellation distributions revealing a large fraction of PIP2 localizations associated with dense DAT localizations (Figures 6A, 6B, and 6F). As seen for DAT nanodomains, treatment with NMDA and haloperidol reduced PIP2 localizations in large dense clusters, whereas haloperidol also reduced cluster size. All of these changes were blocked by AP5 or quinpirole, respectively (Figures 6B–6D). The NMDA- and haloperidol-induced changes were reflected in the Voronoi tessellation distributions as well, showing dispersal of the PIP2 nanodomains and reduced PIP2 association to nanoclustered DAT (Figures 6E and 6F).

The D2R also shows nanodomain distribution

We next analyzed the D2 autoreceptors that are found both in the somatodendritic compartment of DA neurons and in the DA terminals. Because of known challenges with DA receptor antibodies, we validated the specificity of the antibody in transfected HEK293 cells and on slices from D2 receptor knockout mice (Figure S6). Dual-color dSTORM experiments on cultured DA neurons revealed a clustered distribution of the D2 autoreceptors with nanodomains of a similar size as those found for DAT (Figures 7A and 7B). Like our findings for DAT and PIP2, NMDA and haloperidol promoted dispersal of the receptor domains (Figures 7B–7E). Relatively few of the nanodomains, however, overlapped with the DAT domains, as apparent from the Voronoi tessellation distributions (Figures 7A, 7B, and 7F), and, as for D2-autoreceptor association to DAT, we only observed marginal changes upon NMDA and haloperidol treatment (Figure 7F).

The findings prompted us to assess the specificity of the pharmacological manipulations by imaging additional key membrane components in DA terminals, including clathrin (Maxfield and McGraw, 2004) and the single transmembrane soluble N-ethylmaleimide-

sensitive fusion attachment protein receptor (SNARE) protein syntaxin1 (STX-1). Imaging of clathrin revealed a nanoclustered distribution, possibly corresponding to clathrin-coated pits (Li et al., 2018), that showed little co-localization with DAT and, importantly, essentially no change in distribution in response to NMDA (Figure S7). We also recapitulated the nanodomain distribution of STX-1, which is known to exist in such domains in presynaptic terminals (Padmanabhan et al., 2020), as well as the protein has been proposed to bind DAT (Binda et al., 2008). However, the STX-1 domains showed little overlap with DAT and responded differently to NMDA, with a decreased fraction of large clusters and an increased fraction of localizations in dense clusters (Figure S7). NMDA slightly increased localization of STX1 to unclustered DAT (i.e., the larger tessellated areas) according to the Voronoi tesselated distributions (Figure S6). Taken together, several plasma membrane components of DA terminals show a nanoclustered distribution that appears to be differentially regulated.

DISCUSSION

DA neurons have remarkable axonal arbors with numerous presynaptic terminals or varicosities that serve as the principal architectural units responsible for release and reuptake of DA. We still have a surprisingly poor understanding of the regulatory processes taking place in these compartments less than ~1 μm in size. Most of these varicosities are non-synaptic release sites, and it remains unclear whether this results in a less stringent requirement of the spatial organization of the molecular machinery compared with, for example, glutamatergic synapses (Choquet and Hosy, 2020; Groc and Choquet, 2020; Liu and Kaeser, 2019). Here we provide detailed, quantitative insights into how a key membrane protein, DAT, is subject to nanoscale regulation in these varicosities.

As a rough estimate, each DAT nanodomain contains 50–100 DAT molecules, which is in the same range estimated for AMPA receptor domains in the postsynapse (~25 molecules) (Goncalves et al., 2020). Importantly, by using the fluorescent cocaine analog DG3–63 and analyzing the effect of conformationally biased ligands, including noribogaine, JHW007, and nomifensine, we were able to obtain evidence showing that DAT displays a conformational bias depending on whether it is present in a nanodomain or not. This was supported by analyzing the disease-associated DAT mutant D421N, which displays lowered DA affinity and is biased toward an inward-facing conformation. We should note, however, that the distribution of D421N could be affected by the cation leak and anomalous DA efflux that have been associated previously with this mutant (Herborg et al., 2018). Nonetheless, it is appealing to envision that a distribution of DAT between a nanoclustered, inward-facing population of transporter molecules and an unclustered, “free” outward-facing population of DAT molecules represents a means by which DAT activity can be regulated on a fast timescale. A question is whether this dynamic localization of DAT to nanodomains involves changes in DAT oligomerization; however, we find this unlikely, considering recent data supporting that DA dimers are highly stable (Das et al., 2019). Given the large fraction of DAT in nanodomains, it is also unlikely that DAT in nanodomains just constitutes DAT preparing for internalization. But DAT may internalize from the nanodomains as the inward-facing conformation has been associated with internalization (Sorkina et al., 2009).

We validated, in striatal slices, the dispersing effect of excitatory input on DAT nanodomains by employing a Voronoi tessellation-based collection algorithm. In addition to supporting that our findings in cultured DA neurons can be translated to intact tissue, the algorithm offers possibilities for future detailed, quantitative analyses of protein distribution in neuronal terminals in intact brain tissue. Another important observation was a marked role of presynaptic D2R activity, suggesting that the nanoscopic distribution of a membrane protein such as DAT is continuously adapted by several mechanisms to the immediate activity level of the neurons in which it is expressed. It may be considered that the effects of the pharmacological manipulations on DAT clustering are quantitatively modest. However, the effects are highly significant, and it should be considered that the numerous varicosities included in each quantification may be very heterogenous and possibly differentially sensitive to treatment. Such heterogeneity is directly supported by the finding that only a subset of DA terminals appeared to be active at any given time (Pereira et al., 2016).

Our data revealed a striking co-localization of DAT and PIP2 nanodomains. An increase in cytosolic Ca^{2+} has been shown previously to release membrane protein-sequestered PIP2, which might indicate possible PIP2-dependent Ca^{2+} regulation of DAT nanodomain localization (McLaughlin and Murray, 2005). The anionic lipid is known to form nanodomains that have been suggested to be important for membrane protein nanoclustering, including STX-1 (van den Bogaart et al., 2011). Also, both the serotonin transporter (SERT) and DAT bind PIP2 (Buchmayer et al., 2013; Hamilton et al., 2014), and for DAT it has been suggested that PIP2 binds to the DAT N terminus and induces a structural change that encourages phosphorylation and a reverse transport mode of DAT critical for amphetamine-induced DA efflux (Belovich et al., 2019; Hamilton et al., 2014). This is interesting because our data support an inward-facing configuration of nanodomain-localized DAT and, presumably, a more efflux-prone transporter (Robertson et al., 2009). Our previous study indicated a dependency on cholesterol for DAT nanodomain distribution (Rahbek-Clemmensen et al., 2017). Moreover, data have suggested that cholesterol binds to DAT and regulates its function by promoting an outward-facing conformation (Hong and Amara, 2010). A conceivable explanation is that cholesterol serves to compartmentalize the membrane to enable nanoclustered co-distribution of DAT and PIP2 (Carquin et al., 2016; Hwang et al., 1995) and, accordingly, that cholesterol rather interacts with unclustered, outward-facing DAT. It is even possible that rapid movement of DAT in and out of nanodomains parallels the transport cycle shifting the transporter back and forth from an outward-facing, substrate-binding conformation and unclustered distribution to an inward-facing, substrate-releasing (or efflux-prone) conformation and clustered distribution. Our SPT data (SPT-STORM) show that the mean jump distance for a given particle is $r \sim 110$ nm in a 16-ms time frame (Figure 5M), suggesting that a single DAT molecule moves 7–14 μm during a single transport cycle of 1–2 s (Prasad and Amara, 2001). Thus, the movements in the membrane are fast enough for DAT molecules to move in and out of nanodomains during a single transport cycle. Fast movements of DAT have also been supported by classical SPT techniques (Guthrie et al., 2020), although use of large quantum dots for labeling suggested somewhat slower diffusion speeds (Thal et al., 2019).

Previous data have indicated that stimulation of D2 autoreceptors of the D2 and D3 subtype enhances DAT activity (Bolan et al., 2007; Castro-Hernandez et al., 2015; Lee

et al., 2007; Meiergerd et al., 1993; Parsons et al., 1993; Zapata et al., 2007). Here we provide evidence showing that, in DA neuronal cultures, the D2 autoreceptor is preoccupied with DA and that this promotes DAT nanoclustering which is consistent with such an enhancement; that is, if D2-autoreceptor activation causes an increase in DAT activity, then this would expectably lead to a shift of the DAT conformational equilibrium toward a more inward-facing conformation and, hence, a likely shift toward a higher degree of nanodomain localization. However, our data may challenge the theory that regulation of DAT by D2 autoreceptors involves a direct interaction (Bolan et al., 2007; Castro-Hernandez et al., 2015; Lee et al., 2007). Although D2 autoreceptors, like DAT, according to our dSTORM analyses, are distributed into nanodomains, we observed only modest colocalization. The nanodomains responded, nonetheless, like DAT to NMDA and haloperidol, suggesting that excitatory input promotes nanodomain dispersal, whereas D2 autoreceptor activation promotes nanoclustering. We speculate that this increased clustering upon activation reflects assembly of the receptor with intracellular signaling complexes and/or dynamics relating to desensitization and/or internalization.

DAT nanodomains showed rather little co-localization with nanodomains of STX-1 and clathrin, which responded differently to NMDA. These differential effects support that the changes we see for DAT, the D2 autoreceptor, and PIP2 most likely reflect true molecular redistributions and are unlikely to be the result of non-specific changes. The decrease in STX-1 nanocluster size and increased localization within dense clusters in response to NMDA is consistent with other studies indicating that breakup of STX-1 nanodomains, correlating with vesicle release, takes place while more STX-1 is being brought to the sites of release (Maidorn et al., 2019; Padmanabhan et al., 2020). The Voronoi tesselated distributions showed that NMDA slightly increased localization of STX1 to unclustered DAT (i.e., the larger tessellated areas). This suggests that the previously described direct interaction between DAT and STX-1, which has been proposed to be important for amphetamine-induced efflux (Binda et al., 2008), may take place between the unclustered fractions of the two proteins.

In summary, we show compelling evidence that the molecular machinery supporting volume transmission mediated by a neuromodulator like DA is subject to spatial and temporal nanoscale regulation with putative major effect on synaptic function. The results may therefore not only constitute a framework for further deciphering the nanoscale architecture of presynaptic release sites but also add to the growing acknowledgment of nanoscopic regulation as a still poorly explored area of importance for neuronal signaling.

Limitations of the study

We use dopaminergic neurons cultured as our main model system. This is advantageous for analysis of endogenously expressed DAT by super-resolution microscopy. However, our results could deviate from what would be observed in intact tissue. We included data revealing a similar distribution of DAT in striatal slices as well as regulation by NMDA. In some experiments, we use heterologous cells and/or tagged overexpressed constructs. Some of these experiments could not be accomplished in cultured neurons, but the nanoscopic distribution of DAT was similar, so we could still make valid conclusions. Use of dSTORM

for visualization of DAT required permeabilization and fixation, but we controlled for this by application of several different super-resolution techniques, showing similar DAT distribution. Use of several techniques, including ExM, also excluded that the observed distribution of DAT was an artifact because of over-counting (Shivanandan et al., 2014). Moreover, varied label density cluster verification (Baumgart et al., 2016) supported the theory that DAT clustering reflects true nanodomain formation.

STAR⋆METHODS

RESOURCE AVAILABILITY

Lead contact—Further information and requests for resources and reagents should be directed to and will be fulfilled by the Lead Contact, Ulrik Gether (gether@sund.ku.dk).

Materials availability—All unique reagents generated in this study are available from the Lead Contact. Plasmids generated are available upon request.

Data and code availability—The datasets supporting the current study have not been deposited in a public repository because of the file size but are available from the lead author on request.

Custom written codes used for the data analysis can be found at: https://github.com/GetherLab/Super-Resolution-Data-Analysis (https://doi.org/10.5281/zenodo.7016376). The *swift* software was kindly provided by the Ulrike Endesfelder lab, Bonn University. The *swift* version 0.4.3, used in this manuscript, and all subsequent versions, as well as documentation and test data sets, can be obtained at https://swifttracking.slack.com/join/shared_invite/zt-m6e3fb9u-J2~lBX3uaHY0v3JZwiOeSw#/shared-invite/email Any additional information required to reanalyze the data reported in this paper is available from the lead contact upon request

EXPERIMENTAL MODEL AND SUBJECT DETAILS

Primary cultures of rat DA neurons with cortical glia cells—Experimental procedures on adhered to the European guidelines for the care and use of laboratory animals, EU directive 2010/63/EU and were approved by the Danish Animal Experimentation Inspectorate. All efforts were made to minimize animal suffering and to reduce the number of rats used. Cultured glial cells were obtained from cortex and cultured DA neurons were obtained from the midbrain of P1-P3 Wistar rats. Timed pregnancy Wistar IGS rats, day 15, were purchased from Charles River and housed in the animal facility (Department of Experimental Medicine) until pups were born at a normal day cycle with access to standard rodent chow and water ad libitum. The pups were used as described (Klein Herenbrink et al., 2022) at postnatal day 1–2 for generation of cultures of a monolayer of cortical astrocytes with midbrain DA neurons atop. Gender was mixed as the cultures were generated from a mixed sex populations of rat pups. For preparation of cultured glial cells, brains were removed from euthanized P1-P3 pups and placed in phosphate-buffered saline (PBS) on ice. The cortex of each brain was isolated and cut into millimeter sized sections and collected in cold dissection medium (Hanks' Balanced Salt Solution with added Sodium Pyruvate

(1 mM), Penicillin-Streptomycin (Sigma P0781, 200 U/L), 10 mM HEPES, and 0.54% glucose). After collecting all, the dissection medium was replaced with glia cell medium (DMEM with HEPES “1965”, FBS (10%), Penicillin-Streptomycin (60 U/L)). The tissue was mechanically titrated through pipetting up and down using a flame-polished Pasteur pipette followed by straining through a 70 μm cell trainer and centrifugation for 10 min at 200–300 × g. The pellet was resuspended in 10 mL glia medium and strained again before a second centrifugation for 10 min at 200–300 g and removal of the supernatant. The pellet was resuspended and seeded into large T175 flasks at approximately 1.5 brains per flask with added glial medium to a total of 20 mL. Glia cells were grown in an incubator at 37°C with 5% CO_2 until they were 70% confluent. The cells were either frozen in heat-inactivated serum containing 10% DMSO for later use or applied to ethanol-cleaned and poly-D-lysine-coated coverslips and incubated for 1 week prior to DA neuron addition. On the day before DA neuron addition, the glial cells were changed to DA neuron medium (Neurobasal A with heat-inactivated FBS (1/100), GlutaMAX (1/100) B-27 (1/50), ascorbic acid (200 μM), Penicillin-Streptomycin (60 U/L), kynurenic acid (0.5 mM)). Midbrain DA neurons were generated using a protocol modified from Rayport et al., 1992. Brains from rat pups (P1-P3) were isolated and placed in PBS on ice. Midbrain sections were retrieved from each brain as the brains were cut while in dissection buffer. The midbrain sections were transferred to papain solution (cysteine (1 mM), DNase (0.1 mg/mL), papain (20 units/mL), NaCl (116 mM), KCl (5.4 mM), $CaCl_2$ (1.9 mM), NaHCO3 (26 mM), $NaH_2PO_4H_2O$ (2 mM), $MgSO_4$ (1 mM), EDTA (0.5 mM), Glucose (25 mM), kynurenic acid (0.5 mM) in water) for 30 min at 37°C. The solution was replaced with prewarmed DA medium and samples were mechanically titrated with flame polished Pasteur pipettes and the resulting suspension centrifuged at 200–300 × g for 10 min. The pellet was resuspended in DA neuron medium and applied to each culture. Glia-derived neurotrophic factor (GDNF) (100 ng/mL of culture solution volume) was applied immediately after seeding of the neurons. Cultures were incubated for 2 to 3 weeks prior to use.

Mouse brain slices—Experimental procedures on adhered to the European guidelines for the care and use of laboratory animals, EU directive 2010/63/EU and were approved by the Danish Animal Experimentation Inspectorate. All efforts were made to minimize animal suffering and to reduce the number of mice used. Mouse brain slices were obtained from male C57BL/6 mice 12–16 weeks old that were purchased from Scanbur, Denmark and housed in the animal facility (Department of Experimental Medicine) until use at a normal day cycle with access to standard rodent chow and water ad libitum. The slices were prepared as described in Method Details. For validation of D2 receptor antibody, slices were obtained from D2 receptor knock-out mice and WT littermates (Maldonado et al., 1997).

Heterologous cell culture—Cath.a-differentiated (CAD) cells (Qi et al., 1997) (ATCC CRL-11179 or Sigma-Aldrich 08100805), originating from mouse (B6/D2 F1 hybrid) catecholaminergic neuronal tumor. The cells were maintained in a 1:1 mixture of DMEM 1965 and Ham’s F-12 medium (Invitrogen), both supplemented with 10% FBS and 0.01 mg/mL gentamicin. HEK293 cells (human embryonic kidney cells, ATCC CRL-1573) were grown as described (Hansen et al., 2014).

METHOD DETAILS

Molecular biology, virus generation and virus transduction—The cDNA encoding human DAT (synthetic gene kindly provided by Dr. Jonathan Javitch, Columbia University, NY, USA (Loland et al., 2004) was inserted into pmEOS2-C1 (RRID: Addgene#54510) to generate pmEOS2-hDAT C1 encoding hDAT with mEOS2 fused to the N-terminus. Plasmids encoding WT hDAT and D421N hDAT (pRC/CMV hDAT and pRC/CMV hDAT D421N) were generated as described (Herborg et al., 2018). The cDNA encoding the short transcriptional variant of human DA D2 receptor with an N-terminal FLAG tag (SF-D2R-S) was inserted into mammalian expression vector pcDNA 3.1(+) (Invitrogen) (Klewe et al., 2008). The Cre-dependent construct, pAAV-CAG-Flex-NES-jRGECO1a-WPREpA, was obtained from Addgene (RRID: Addgene #100854). The plasmids, pAAV-hSyn-DIO-mNaChBac-T2A-mKate2-WPREpA, pAAV-hSyn-DIO-mNaChBacMUT-T2A-mKate2-WPREpA and pAAV-hSyn-DIO-Kir2.1-T2A-mKate2-WPREpA (Lin et al., 2010; Xue et al., 2014), were SLIC cloned (Jeong et al., 2012) from pAAV-EF1α-F-FLEX-mNaChBac-T2A-tdTomato (RRID: Addgene #60658) and pAAV-EF1α-F-FLEX-Kir2.1-T2A-tdTomato (RRID: Addgene #60661), respectively, into a Cre-dependent AAV backbone plasmid with a mKate2 fluorophore instead of tdTomato. This was done to make them sufficiently short so that packaging into an AAV capsid would be feasible (ITR to ITR length<4700 kbp). The pAAV-pTH-iCre-WPREpA construct was created and cloned in-house and contains a truncated 488 bp rat TH promoter encoding Cre recombinase. In-house generated AAVs were produced using a FuGene6 (Promega) mediated triple plasmid co-transfection method in HEK293t cells. Three days after transfection, cells were harvested and virus purified using an adapted Iodixanol gradient purification protocol (Matsui et al., 2012). Genomic AAV titer was determined by a PicoGreen-based method as described elsewhere (Piedra et al., 2015). AAV2-retro-pTH-iCre mediated expression of Cre-dependent jRGECO1 was verified by fluorescence microscopy and no differences were observed across the different titers used. For transduction, the appropriate virus was applied to primary culture DA neurons at an approximate concentration of 2*10E9 vg/mL at 1 to 3 days after preparation of the neuronal cultures.

Transfection of DA neurons—Primary cultures of DA neurons were transfected using Magnetotransfection at ~14 DIV (Underhill et al., 2014). NeuroMag reagent (OZ biosciences) (8 μL) was mixed with plasmid (4 μg) and DA neuron medium (200 μL). The mixture was incubated for 20 min at RT before it was added to cultures grown in 6-well plates. The culture was positioned on top of a magnetic plate for 15 min after which the culture before it was moved back to the cell incubator and used for immunostaining 24–48 h later.

Immunostaining of primary cultures of DA neurons for dSTORM and PALM—The cell samples were fixed in paraformaldehyde (3%) and washed three times in glycine (20 mM) and NH_4Cl (50 mM) in PBS. Subsequently, the cells were washed in blocking buffer (5% Donkey serum, 1% BSA in PBS), and incubated in blocking permeabilization buffer (blocking buffer with saponin (0.2%)). Primary antibody was applied in blocking buffer for 60 min, followed by 3–5 min incubation in blocking buffer. Secondary antibody was applied in blocking buffer for 45 min, and the sample was incubated 2x for 5 min in

blocking buffer. Samples were washed in PBS twice and post-fixated in paraformaldehyde (3%) for 15 min. Samples were washed twice in glycine (20 mM) and NH_4Cl (50 mM) in PBS and stored in PBS at 4°C until imaging.

The synaptotagmin 1 feeding experiment was performed as defined by Truckenbrodt et al., 2018. Live DA primary cultures were exposed to synaptotagmin 1 antibody (SS 105 311, Synaptic Systems) at a 1:120 dilution from a 1 mg/mL solution together with haloperidol (10 nM) or vehicle 37°C for one hour. The cultures were carefully washed with 37°C aCSF while avoiding exposure to air before fixation and immunolabeling per the primary culture staining protocol.

Preparation and immunostaining of mouse brain slices for dSTORM—Mice were anesthetized with isoflurane and perfused first with PBS followed by 4% paraformaldehyde (PFA) injected directly into the heart. Brains were then placed in 4% PFA for 24 h, followed by sucrose (30%) for 24 to 48 h. Subsequently, brains were snap-frozen on powdered dry ice and stored at −80°C. The brains were sliced using a cryostat (Leica CM3050 S) to obtain 10 μm striatal coronal sections and each slice was immediately fused to a 3-aminopropyltriethoxysilane coated coverslip and let dry at room temperature before being stored in antifreeze (50% glycerol 50% PBS) at −20°C. For immunostaining, brain sections were first rinsed 3x in PBS and subsequently washed 2x with 15 min incubation in glycine (20 mM) and NH_4Cl (50 mM) in PBS. This was followed by 30 min wash in 10 mM trisodium citrate, pH 6.0, preheated to 80°C, 4x wash in PBS and then blocking/permeabilization for 30 min in PBS with 5% donkey serum, 1% BSA and 0.3% Triton X-100. Primary antibody was applied overnight in blocking/permeabilization buffer followed by washing in 5/5/90 min increments and application of secondary antibody overnight in blocking/permeabilization buffer. Sections were again washed in 5/5/90 min increments in blocking/permeabilization buffer and then with 5/5 min increments with PBS. The sections were post-fixated in paraformaldehyde (3%) and washed twice for 15 min in glycine (20 mM) and NH_4Cl (50 mM) in PBS. Samples were lastly washed twice in PBS and stored in PBS at 4°C until imaging.

Antibodies and labeling—Secondary antibodies (donkey anti-rat, Jackson 712-005-153, RRID:AB_2340631; donkey anti-mouse, Jackson 715-005-151, RRID:AB_2340759); or donkey anti-rabbit, Jackson 711-005-152, RRID:AB_2340585) were labeled with either NHS-ester conjugated Alexa 647 or CF™568 (Biotium, Freemont, CA) and then isolated through Zeba™ Spin Desalting Columns, 40K MWCO (ThermoFisher 87767). This was completed by first washing the column 3x with 300 μL of 100 mM $NaHCO_3$ in PBS. Following the washes, 50 μg of antibody in 100 μL of PBS was added and spun at 1500 × g for 2 mins. The flow-through was collected and combined with a 5-fold molar excess of NHS ester fluorophore. This solution was incubated in the dark at RT, shaking, for 2.5 h. A new spin column was then washed 3 times with NaN–3 (0.02%) in PBS. The antibody sample with the dye was then added to the column and centrifuged for 2 min at 1500 × g. The protein concentration and label concentration of the final product were measured on a NanoDrop 2000 Spectrophotometer (ThermoFisher). Labeled antibodies had between 1 and 2 fluorophores attached.

We used the following antibodies and fluorophores for our imaging analysis: DAT, Millipore MAB369 RRID:AB_2190413, Primary culture dSTORM, 1/200, 5 μg/mL Donkey anti-Rat, Alexa647; DAT, Millipore MAB369 RRID:AB_2190413, IHC dSTORM, 1/200, 10 μg/mL Donkey anti-Rat Alexa647; DAT, Millipore MAB369 RRID:AB_2190413, Expansion (ExM), 1/200, 5 μg/mL Donkey anti-Rat Atto 643; TH, Millipore MAB318 RRID:AB_2201528, PALM/dSTORM 1/500, 5 μg/mL Donkey anti-Mouse Alexa647; STX-1, Synaptic Systems 110 011 RRID:AB_887844, Primary culture dSTORM, 1/500, 5 μg/mL Donkey anti-Mouse CF568; Clathrin light chain, Synaptic Systems 113 011 RRID:AB_887706, Primary culture dSTORM, 1/500, 5 μg/mL Donkey anti-Mouse CF568; PIP2, Abcam ab11039 RRID:AB_442848, Primary culture dSTORM, 1/500, 5 μg/mL Donkey anti-mouse CF568; D2R, Synaptic Systems 376 205 RRID:AB_2636918, Primary culture dSTORM, 1/500, 5 μg/mL Donkey anti-rabbit, CF568; mKate2, Evrogen AB233 RRID:AB_2571743, Primary culture dSTORM, 1/500, 5 μg/mL Donkey anti-rabbit CF568; Synaptotagmin 1 (luminal domain), Synaptic systems 105 311 RRID:AB_10805653; Active varicosity detection, 1/125, 5 μg/mL Donkey anti-Mouse Alexa 488.

Expansion microscopy (ExM)—For ExM, perfused brains were acquired by injecting first PBS and then 4% PFA into the heart of anesthetized mice. Brains were postfixated in 4% PFA for 24 h and immersed in sucrose solution (30%) for 24 to 48 h. Coronal brain slices (40 μm) were obtained with a cryostat. The brain slices were stored, free floating, in antifreeze (50% glycerol 50% PBS) at −20°C until use. Brain slices were washed with PBS three times, and then permeabilized in blocking buffer (5% donkey serum, 1% bovine serum albumin, 0.1% Triton X-100, in PBS). Brain slices were incubated overnight with primary antibody in blocking buffer (5% donkey serum, 1% bovine serum albumin, 0.1% Triton X-100, in PBS, pH 7.4). Slices were washed 4x in blocking buffer with 30 min increments and incubated overnight with secondary antibody in blocking buffer at 4°C. Slices were again washed 4x in blocking buffer with 30 min increments. Anchoring treatment was performed with Acryloyl-X-SE (0.1 mg/mL) in PBS at room temperature overnight (Truckenbrodt et al., 2019). Gel solution was made by mixing N,N-dimethylacrylamide (1.335 g) and sodium acrylate (0.32 g) in 2.85 g of water. Oxygen was purged with nitrogen gas for 40 min 2.7 mL of the gelling solution were mixed with 0.3 mL 0.036 g/mL solution of potassium persulfate ($K_2S_2O_8$) solution and purged of oxygen with nitrogen gas for 15 min on ice. Brain slices were transferred to the extra gelling solution and placed flat on poly-D-Lysine coated glass slides. . Excess gelling solution was removed, and glass coverslips were placed on the edges of each slice to limit gel dispersion. All work from this point was done in a cold room (4°C). Aliquots of 500 μL of polymerization solution were combined with 2 μL of TEMED was added and the solution vortexed before applying 80 μL to brain slices. A layer of parafilm covered coverslip was placed overtop of the gel to fully surround the gel. The sample was kept in the cold room for 15 min before being brought back out to room temperature. The container with the gels was filled with nitrogen and wet paper to keep humidity and made airtight. Following gelation, samples were carefully cut out from the chamber in a sim-card shape to ensure orientation. Gels were measured in size, and placed in digestion buffer overnight at room temperature (50 mM TRIS, 800 mM guanidine HCl, 2 mM CaCl2, 0.5% Triton X-100, proteinase K 8 U/mL, pH 8.0). The gels were placed into individual dishes and dialyzed with water many

times over a day until they no longer expanded. Imaging was performed the next day on a spinning disk confocal microscope (FEI CorrSight utilizing a C-Apochromat 63x/1.20 W Corr M27 objective). Samples were places dry on poly-D-Lysine coated chambers and water was added to the top of the gel just enough so the gel was hydrated but not so it would move around.

dSTORM—For dSTORM we used a buffer containing β-mercaptoehtanol and an enzymatic oxygen scavenger system (10% (w/V) glucose, 1% (V/V) beta-mercaptoethanol, 2 mM cyclooctatetraene, 50 mM Tris-HCl (pH 8), 10 mM NaCl, 34 μg mL^{-1} catalase, 28 μg mL^{-1} glucose oxidase). The imaging was performed with an ECLIPSE Ti-E epifluoresence/TIRF microscope (NIKON, Japan) equipped with 405 nm, 488 nm, 561 nm, and 647 nm lasers (Coherent, California, USA). All lasers are individually shuttered and collected in a single fiber to the sample through a 1.49 NA, 100x, apochromat TIRF oil objective (NIKON). Single color imaging was done with a dichroic mirror (z405/488/561/647 rpc) and the emitted light was filtered by a 710/80 nm bandpass filter. For dual-color dSTORM, we used a dichroic mirror with the range 350–412, 485–490, 558–564, and 637–660 nm (97,335 QUAD C-NSTORM C156921). The excitation light was filtered at the wavelengths: 401 ± 24 nm, 488 ± 15 nm, 561 ± 15 nm, 647 ± 24 nm. The emitted light was filtered at the wavelengths: 425–475, 505–545, 578–625, and 664–787 nm, and secondly by an extra filter to decrease noise (561 nm Longpass, Edge Basic, F76–561, AHF). A motorized piezo stage controlled by a near-infrared light-adjusted perfect focus system (NIKON) is applied to the system to reduce any sample drift over time in the z-direction. Single-color dSTORM images were constructed from 30,000 frames taken at a 16 ms frame rate. Dual-color dSTORM images were constructed from 20,000 frames for each color taken at a 16 ms frame rate with each color alternating by frame. Photons were collected with an iXon3 897 EM-CCD camera camera (Andor, United Kingdom). Laser powers used were 2.3 kW cm −2 for 647 nm, 1.0 kW cm−2 for 488 nm and for 561 nm. The 405 nm laser was used to incrementally increase blinking behavior at power <0.1 kW cm−2. For 3D-dSTORM, a cylindrical lens was placed before the camera to impart astigmatism.

PALM—For PALM imaging of mEos-DAT, we obtained 5,000 consecutive frames with a frame rate of 33 Hz to construct one image. The 488 nm excitation laser was held constant, 0.4 kW cm^{-2}, during the capture of the image while the 405 nm activation laser was gradually increased to <0.1 kW cm^{-2}.

Localization fitting of dSTORM data—2D localizations were fit with ThunderSTORM using local maximum detection with a threshold of 1.5 *std(Wave.F1) and estimator of an integrated gaussian PSF. Sigma was 1.6, fit radius was 3 pixels, and weighted least squares was the method to fit the estimated gaussian to the PSF (Ovesny et al., 2014). 3D localization fitting was performed with fit3Dcspline (Li et al., 2018). 3D calibrations were made on 100 nm TetraSpeck beads attached to a coverslip by first placing 50 μL of MgCl2 (1 M) on the coverslip and then adding 500 L of water with 0.9 μL of TetraSpeck beads to the coverslip. Drift for all data was corrected with redundant cross correlation through Matlab (Wang et al., 2014). Localizations were filtered for uncertainty being less than 25 nm and then merged for localizations that were detected within 15 nm and 3 frames.

Data processing pipeline - dSTORM—To perform necessary localization fitting on the 1349 dSTORM images included in this study, an in-house data processing pipeline was developed to streamline operations. Localizations were fit to the raw data with the aforementioned settings in ThunderSTORM through a self-written ImageJ macro. Although ThunderSTORM can perform the remaining processing steps, a custom python script (utilizing Matlab functions) was written to perform cross correlation, merging and filtering so that redundant cross correlation could be employed. The images were then blinded by labeling them with a random integer and saving the cypher elsewhere. Through a separate custom Matlab script, varicosities were selected from each image though a freehand selection. Varicosities were identified by the local swelling of their structure compared to the rest of the extension. We next used DBSCAN (density based spatial clustering of applications with noise) (Ester et al., 1996; Rahbek-Clemmensen et al., 2017) to identify clusters by size or for determining localizations in dense clusters through the use of a python script employing the DBSCAN method from the sklearn python library. Voronoi tessellation (Levet et al., 2019) was employed through Matlab. The Voronoi based density association algorithm was also written in house and using Matlab.

Varicosity identification in dSTORM DA neuron culture data—Automatic varicosity identification could not discern between extension and varicosity, so these were selected through a freehand ROI taken of blinded files. Localization data for all images in a given dataset were blinded by being randomly assigned a number that was stored on a cypher. ROIs were then gathered without the knowledge of the image identity, with this information restored in the analysis of the ROIs.

Varicosity identification in brain slice dSTORM data—As this was a computationally intensive process, each image was divided into 100 quadrants in a 10×10 grid. Within each quadrant, the localizations were sub-sampled down to 1000 random localizations, and the Voronoi tessalation was obtained for that section. Tesselated areas were filtered for having an area less than 15000 nm^2. Tesselated shapes that were touching one another were merged together. Shapes were now filtered for possessing an area greater than 300000 nm^2. These ROIS were buffered by 50 nm along each edge to smooth the ROI.

Clustering analysis of dSTORM data—Cluster size was identified by performing DBSCAN on each varicosity for a radius of 15 nm and 5 localizations being the cluster qualifier. The convex hull was gathered for each cluster to find its area, and the fraction of clusters with a diameter >75 nm was used for the cluster size analysis. Cluster size distributions were not shown as clusters reaching the detection limit of this method are not accurate and cause a false perception on the cluster size distribution. Localizations in dense clusters were found by applying DBSCAN to each varicosity with a radius of 50 nm and 80 localizations being the qualifier. Voronoi tessellation was applied to each varicosity and areas were filtered for sizes between 5 nm2 and 1000 nm2. Probability density functions were created for these distributions.

Density association—Density association was found by performing Voronoi tessellation on target A, and finding all points in target B that were 25 nm from any point in target

A. Each of these target B points that possessed A association were mapped to the Voronoi tessellated area from target A they resided in. The probability density functions for target A and the areas from target A that had an associated target B were created.

This procedure was applied to compare the dSTORM signal of DG3_63 to mEOS2-DAT, STX1 to DAT, D2R to DAT, PIP2 to DAT, and clathrin to DAT.

Quantification of DAT molecules in nanodomains—Primary DA neurons were labeled and imaged for dSTORM with the DAT MAB369 antibody at dilutions 1:200, 1:400, 1:800, 1:1600, 1:3200. Varicosities were manually selected from blinded data files. Clusters of localizations potentially arising from single localizations were identified in the varicosities found in the 1:3200 dilution data set through DBSCAN with the parameters [ε = 30 nm, nps = 2]. A histogram was made comparing the number of localizations found per cluster from this cluster analysis, and 3 localizations was determined to be the estimate for the number of localizations arising from a single monoclonal antibody in this image set. Clusters were then found in the remaining dataset through the same method defined to identify cluster size. A histogram was made to show the number of localizations present within the clusters found with a diameter >75 nm. The peak of this histogram was ~100 localizations, suggesting there are roughly 33 primary antibodies labeling DAT within a given cluster/nanodomain of this size.

Varied label density cluster verification—Varicosities used for the counting experiment were subject to the varied label density cluster verification test (Baumgart et al., 2016). Sig for gaussians was set to 15 nm and the cut gauss at x times sig was set to 2. The threshold selected was 2.

Labeling and imaging primary cultures with DG3–63—Live primary cultures were labeled with DG3–63 (20 nM) (Guthrie et al., 2020) for 10 min in the dark at room temperature and washed 3 times with aCSF (NaCl (120 mM), KCl (5 mM), $CaCl_2$ (2 mM), $MgCl_2$ (2 mM), 1 mM NaH_2PO_4, HEPES (25 mM), glucose (30 mM), pH 7.4). Samples were fixed with paraformaldehyde (3%) for 15 min followed by 3 washes with glycine (20 mM) and NH_4Cl (50 mM) in PBS. Samples were imaged in normal dSTORM buffer.

Transfection of CAD cells, labeling with DG3–63 and pharmacological treatments—CAD cells were transfected with pmEOS2-hDAT encoding mEOS-DAT or with pRC/CMV-hDAT or pRC/CMV-hDAT D421N encoding WT DAT and the DAT mutant D421N, respectively (Herborg et al., 2018). The CAD cells (~1 million cells) were seeded the day before transfection in a 25 cm^2 flask and washed on the day of transfection before addition of 5 mL of medium. For the transfection, 1 μg of DNA was added to 100 μL of optiMEM as well as 3 μL Lipofectamine (Invitrogen) to a separate 100 μL of optiMEM. After 5 min, the two solutions were mixed and incubated for 30 min before the total mixture was added to the cells. The next day the cells were harvested and seeded on poly-D-Lysine coated coverslips (100,000 cells per coverslip). For DG3–63 labeling experiments, the media was removed the next day from the mEOS-DAT expressing cells and 1 mL of aCSF was added (NaCl (120 mM), KCl (5 mM), $CaCl_2$ (2 mM), $MgCl_2$ (2 mM), HEPES (25 mM), glucose (30 mM), pH 7.4) before incubation for 10 min with or without 100 μM unlabeled

cocaine. Following this, the cells were labeled with 10 nM DG3–63 (Guthrie et al., 2020) for 10 min in aCSF. Samples were washed 3 times with aCSF and then fixed for 15 min in paraformaldehyde (3%) followed by 2x wash with glycine (20 mM) and NH_4Cl (50 mM) in PBS. Samples were imaged in dSTORM buffer as described above. For dSTORM of hDAT WT and D421N, cells the cover slips samples were stained in the same fashion as primary DA cultures. For pharmacology experiments, CAD cells expressing WT DAT were treated with nomifensine (20 μM), noribogaine (20 μM), JHW007 (20 μM) or vehicle for 10 min prior to fixation.

Pharmacological treatment of acute brain slices—Mice were euthanized with isoflurane and the live brains were removed. Coronal sections, 300 μm thick, were cut with a vibratome in cold aCSF (NaCl (119 mM), KCl (2.5 mM), NaH_2PO_4 (24 mM), Glucose (12.5 mM), $CaCl_2$ (2 mM), $MgCl_2$ (2 mM)) that was being aerated with carbogen gas. Brain slices were transferred to aCSF and maintained for 1 h at room temperature under constant carbogenation. Slices were then transferred to either aCSF or aCSF with AP5 (100 μM), both at 37°C for 10 min. Slices from normal aCSF were moved to aCSF with or without NMDA (20 μM). The NMDA containing aCSF had reduced magnesium (0.3 mM MgCl2) and added glycine (100 μM). The samples from AP5 were transferred to aCSF with AP5 (100 μM) and NMDA (20μM), reduced magnesium (0.3 mM $MgCl_2$), and added glycine (100 μM). These incubated for 5 min, and then the slices were transferred to paraformaldehyde (3%) overnight at 4°C. Slices were transferred to a 30% sucrose solution for 2 days a 4°C and then placed into plastic molds and covered with Tissue-Tek O.C.T. and stored at −80°C. Samples were sliced at 10 μm on the cryostat and stained for dSTORM.

Pharmacological treatment of primary cultures—In general, treatments were performed by replacing the media at room temperature with aCSF (NaCl (120 mM), KCl (5 mM), $CaCl_2$ (2 mM), $MgCl_2$ (2 mM), 1 mM NaH_2PO_4, HEPES (25 mM), glucose (30 mM), pH 7.4) followed by stimulation with indicated compounds. For the NMDA or haloperidol experiments with testing of VGCC inhibitors, cells were treated for 10 min with either control aCSF, AP5 (100 μM) or quinpirole (50 μM), ω-conotoxin (1 μM), ω-agatoxin (1 μM). Samples were then treated for 5 min with these same concentrations as cotreatment with either NMDA (20 μM) or haloperidol (10 nM). NMDA treatments were done in aCSF with added glycine (100 μM). All experiments using NMDA were done with aCSF with reduced magnesium (0.3 mM $MgCl_2$) for all conditions. For the BAPTA-AM experiment, the pretreatment with BAPTA-AM (25 μM) was for 30 min prior to the 5-min NMDA (20 μM) treatment. For the DAT pharmacology experiments, the neurons were treated for 5 min with either nomifensine (10 μM), noribogane (20 μM) or dopamine (200 nM) prior to fixation.

SPT-dSTORM—Live primary cultures were labeled with DG3–80 (20 nM) for 10 min and then washed 3 times with aCSF (NaCl (120 mM), KCl (5 mM), $CaCl_2$ (2 mM), $MgCl_2$ (2 mM–0.3 mM for NMDA related experiments), 1 mM NaH_2PO_4, HEPES (25 mM), glucose (30 mM), pH 7.4). A suitable location to image was found while the sample was kept in aCSF, and then SPTdSTORM imaging was done in a modified dSTORM buffer (560 μg/mL glucose oxidase, 34 μg/mL catalase, 1.4 μL/mL β-Mercaptoethanol in aCSF).

Pharmacological treatment were done 5 min before imaging with either 20 μM NMDA with 100 μM glycine, 200 nM haloperidol, or 1 μM UH-232. AP5 (100 μM) was applied for 10 min prior to cotreatment with NMDA. Imaging was performed at room temperature on the NIKON TiE Eclipse TIRF microscope described under dSTORM. Light with a wavelength of 561 nm at 0.3 kW cm^{-2} was utilized to promote blinking of the fluorophores. Images were collected with 16 ms frame rate. Localizations were fit using ThunderStorm as described above. Single molecule trajectories were found using the program swift (Turkowyd et al., 2020). Parameter used beyond the default were: “expdisplacement”: 300,”expnoiserate”: 10,”maxblinkingduration”: 2,”pblink”: 0.5,”preappear”: 0.5,”pswitch”: 0.001,”precision”: 30,”pruningbase”: 2,”pruningrate”: 0.2,”randomseed”: 42,”wdiffusion”: 2,”wdirected”: 1,”wfield”: 0,”wimmobile”: 1.

Electrophysiology recordings of DA neurons—DA neuronal cultures were transduced after 3 DIV (days *in vitro*) with pAAV-pTH-iCre-WPREpA plus either pAAV-hSyn-DIO-mNaCh-Bac-T2A-mKate2-WPREpA, pAAV-hSyn-DIO-mNaChBacMUT-T2A-mKate2-WPREpA or pAAV-hSyn-DIO-Kir2.1-T2A-mKate2-WPREpA. Electrophysiological recording by the whole-cell patch clamp technique were done 2–3 weeks after transduction. The DA neurons expressing either mNaChBac or Kir2.1 were identified based on mKate2 fluorescence using an upright microscope (Olympus BX51WI). For the recordings, the cultures were submerged in circulating, heated, and oxygenated aCSF (in mM; NaCl 125, KCl 2.5, $NaHCO_3$ 26, $CaCl_2$ 2, $MgCl_2$ 1, NaH_2PO_4 1.25, Glucose 25; 2 mL/min, 35°C). The aCSF was supplemented with NBQX (20 μM). The patch glass electrode was filled with (in mM) K-gluconate 122, Na_2-ATP 5, $MgCl_2$ 2.5, $CaCl_2$ 0.0003, Mg-Gluconate 5.6, K-Hepes 5, H-Hepes 5, and EGTA 1, and had tip resistance of 4–6 MΩ. After break-in, the cells were held at 0 pA in current clamp mode to measure the pacemaker activity. Recordings were acquired with a Multiclamp 700B amplifier and 1440A Digitizer.

Calcium imaging of DA neurons—Primary DA neurons were prepared as described above but instead of culturing the neurons on glass coverslips, they were cultured on MatTek 35 mm 14 mm glass microwell (no 1.5) glass bottom dishes (MatTek). To enable measurement of Ca^{2+}-fluctuations specifically in DA neurons, the neurons were transduced with an AAV encoding double-floxed jRGECO1a (AAV-CAG-Flex-NES-jRGECO1a-WPREpA) together with an AAV encoding Cre recombinase under control of a truncated TH promoter (AAV2-retro-pTH-iCre-WPREpA). The cell medium was changed to aCSF (NaCl (120 mM), KCl (5 mM), CaCl2 (2 mM), $MgCl_2$ (2 mM), 1 mM NaH_2PO_4, HEPES (25 mM), glucose (30 mM), pH 7.4) immediately prior to imaging. Imaging took place at room temperature on the NIKON TiE Eclipse TIRF microscope described above. Once a suitable neuron was located, the sample was imaged with 561 nm light (10 W cm^{-2}). Videos were collected with a 16 ms frame rate. Haloperidol was added mid-video so that the sample had a total concentration of 10 nM Haloperidol. Data was collected from three independent experiments. Two varicosities were identified per image.

RNA-seq mining and data analysis—All RNA sequencing data was accessed via the Gene Expression Omnibus (GEO) under the following accession numbers: GSE108020,

GSE115070, GSE76381, GSE116470, GSE116138. Raw counts were converted to RPKM and quantile normalized using the preprocessCore (3.11) package in R.

QUANTIFICATION AND STATISTICAL ANALYSIS

Statistical details can be found in the figure legends and were computed with GraphPad Prism 8. When employing one-way ANOVA, Dunnett's post hoc test was used for multiple comparisons. The dSTORM comparisons were normalized to the control sample from the individual imaging session. This was done to control for unavoidable variability in sample preparations and between imaging sessions. Please see Table S1 for details on numbers of sample preparations, dSTORM images and varicosities analyzed in the individual experiments.

Supplementary Material

Refer to Web version on PubMed Central for supplementary material.

ACKNOWLEDGMENT

We thank Ralph Götz for support with expansion microscopy and Dr. Emiliana Borrelli for providing tissue from D2R knockout mice. The work was supported by Lundbeck Foundation grants R266-2017-4331 (to U.G.), R276-2018-792 (to U.G.), R230-2016-3154 (to M.D.L.), R181-2014-3090 (to F.H.), R303-2018-3540 (to F.H.), and R231-2016-2481-5 (to A.T.S.); Independent Research Fund Denmark – Medical Sciences (7016-00325B to U.G.); and NIDA-Intramural Research Program Z1A DA000610 (to A.H.N. and D.A.G.).

REFERENCES

Baker SM, Buckheit RW 3rd, and Falk MM (2010). Green-to-red photoconvertible fluorescent proteins: tracking cell and protein dynamics on standard wide-field mercury arc-based microscopes. BMC Cell Biol. 11, 15. 10.1186/1471-2121-11-15. [PubMed: 20175925]

Baumgart F, Arnold AM, Leskovar K, Staszek K, Fölser M, Weghuber J, Stockinger H, and Schütz GJ (2016). Varying label density allows artifact-free analysis of membrane-protein nanoclusters. Nat. Methods 13, 661–664. 10.1038/nmeth.3897. [PubMed: 27295310]

Beckstead MJ, Grandy DK, Wickman K, and Williams JT (2004). Vesicular dopamine release elicits an inhibitory postsynaptic current in midbrain dopamine neurons. Neuron 42, 939–946. 10.1016/j.neuron.2004.05.019. [PubMed: 15207238]

Belovich AN, Aguilar JI, Mabry SJ, Cheng MH, Zanella D, Hamilton PJ, Stanislowski DJ, Shekar A, Foster JD, Bahar I, et al. (2019). A network of phosphatidylinositol (4, 5)-bisphosphate (PIP2) binding sites on the dopamine transporter regulates amphetamine behavior in Drosophila Melanogaster. Mol. Psychiatry 26, 4417–4430. 10.1038/s41380-019-0620-0. [PubMed: 31796894]

Bermingham DP, and Blakely RD (2016). Kinase-dependent regulation of monoamine neurotransmitter transporters. Pharmacol. Rev. 68, 888–953. 10.1124/pr.115.012260. [PubMed: 27591044]

Beuming T, Kniazeff J, Bergmann ML, Shi L, Gracia L, Raniszewska K, Newman AH, Javitch JA, Weinstein H, Gether U, and Loland CJ (2008). The binding sites for cocaine and dopamine in the dopamine transporter overlap. Nat. Neurosci. 11, 780–789. 10.1038/nn.2146. [PubMed: 18568020]

Binda F, Dipace C, Bowton E, Robertson SD, Lute BJ, Fog JU, Zhang M, Sen N, Colbran RJ, Gnegy ME, et al. (2008). Syntaxin 1A interaction with the dopamine transporter promotes amphetamine-induced dopamine efflux. Mol. Pharmacol. 74, 1101–1108. 10.1124/mol.108.048447. [PubMed: 18617632]

Björklund A, and Dunnett SB (2007). Dopamine neuron systems in the brain: an update. Trends Neurosci. 30, 194–202. 10.1016/j.tins.2007.03.006. [PubMed: 17408759]

Bolan EA, Kivell B, Jaligam V, Oz M, Jayanthi LD, Han Y, Sen N, Urizar E, Gomes I, Devi LA, et al. (2007). D2 receptors regulate dopamine transporter function via an extracellular signal-regulated kinases 1 and 2-dependent and phosphoinositide 3 kinase-independent mechanism. Mol. Pharmacol. 71, 1222–1232. 10.1124/mol.106.027763. [PubMed: 17267664]

Borroto-Escuela DO, Perez De La Mora M, Manger P, Narváez M, Beggiato S, Crespo-Ramírez M, Navarro G, Wydra K, Díaz-Cabiale Z, Rivera A, et al. (2018). Brain dopamine transmission in health and Parkinson's disease: modulation of synaptic transmission and plasticity through volume transmission and dopamine heteroreceptors. Front. Synaptic Neurosci. 10, 20. 10.3389/fnsyn.2018.00020. [PubMed: 30042672]

Buchmayer F, Schicker K, Steinkellner T, Geier P, Stübiger G, Hamilton PJ, Jurik A, Stockner T, Yang J-W, Montgomery T, et al. (2013). Amphetamine actions at the serotonin transporter rely on the availability of phosphatidylinositol-4, 5-bisphosphate. Proc. Natl. Acad. Sci. USA 110, 11642–11647. 10.1073/pnas.1220552110. [PubMed: 23798435]

Carquin M, D'Auria L, Pollet H, Bongarzone ER, and Tyteca D (2016). Recent progress on lipid lateral heterogeneity in plasma membranes: from rafts to submicrometric domains. Prog. Lipid Res. 62, 1–24. 10.1016/j.plipres.2015.12.004. [PubMed: 26738447]

Castro-Hernández J, Afonso-Oramas D, Cruz-Muros I, Salas-Hernández J, Barroso-Chinea P, Moratalla R, Millan MJ, and González-Hernández T (2015). Prolonged treatment with pramipexole promotes physical interaction of striatal dopamine D3 autoreceptors with dopamine transporters to reduce dopamine uptake. Neurobiol. Dis. 74, 325–335. 10.1016/j.nbd.2014.12.007. [PubMed: 25511804]

Chen F, Tillberg PW, and Boyden ES (2015). Optical imaging. Expansion microscopy. Science 347, 543–548. 10.1126/science.1260088. [PubMed: 25592419]

Choquet D, and Hosy E (2020). AMPA receptor nanoscale dynamic organization and synaptic plasticities. Curr. Opin. Neurobiol. 63, 137–145. 10.1016/j.conb.2020.04.003. [PubMed: 32416471]

Das AK, Kudlacek O, Baumgart F, Jaentsch K, Stockner T, Sitte HH, and Schütz GJ (2019). Dopamine transporter forms stable dimers in the live cell plasma membrane in a phosphatidylinositol 4, 5-bisphosphate-independent manner. J. Biol. Chem. 294, 5632–5642. 10.1074/jbc.RA118.006178. [PubMed: 30705091]

Descarries L, Watkins KC, Garcia S, Bosler O, and Doucet G (1996). Dual character, asynaptic and synaptic, of the dopamine innervation in adult rat neostriatum: a quantitative autoradiographic and immunocytochemical analysis. J. Comp. Neurol. 375, 167–186. 10.1002/(SICI)1096-9861(19961111)375:2<167::AID-CNE1>3.0.CO;2-0. [PubMed: 8915824]

Ehmann N, van de Linde S, Alon A, Ljaschenko D, Keung XZ, Holm T, Rings A, DiAntonio A, Hallermann S, Ashery U, et al. (2014). Quantitative super-resolution imaging of Bruchpilot distinguishes active zone states. Nat. Commun. 5, 4650. 10.1038/ncomms5650. [PubMed: 25130366]

Eriksen J, Jørgensen TN, and Gether U (2010). Regulation of dopamine transporter function by protein-protein interactions: new discoveries and methodological challenges. J. Neurochem. 113, 27–41. 10.1111/j.1471-4159.2010.06599.x. [PubMed: 20085610]

Ester M, Kriegel H-P, Sander J, and Xu X (1996). A density-based algorithm for discovering clusters in large spatial databases with noise. In Proc. 2nd International Conference on Knowledge Discovery and Data Mining (AAAI Press), pp. 226–231.

German CL, Baladi MG, McFadden LM, Hanson GR, and Fleckenstein AE (2015). Regulation of the dopamine and vesicular monoamine transporters: pharmacological targets and implications for disease. Pharmacol. Rev. 67, 1005–1024. 10.1124/pr.114.010397. [PubMed: 26408528]

Giguère N, Delignat-Lavaud B, Herborg F, Voisin A, Li Y, Jacquemet V, Anand-Srivastava M, Gether U, Giros B, and Trudeau LÉ (2019). Increased vulnerability of nigral dopamine neurons after expansion of their axonal arborization size through D2 dopamine receptor conditional knockout. PLoS Genet. 15, e1008352. 10.1371/journal.pgen.1008352. [PubMed: 31449520]

Goncalves J, Bartol TM, Camus C, Levet F, Menegolla AP, Sejnowski TJ, Sibarita JB, Vivaudou M, Choquet D, and Hosy E (2020). Nanoscale co-organization and coactivation of AMPAR, NMDAR, and mGluR at excitatory synapses. Proc. Natl. Acad. Sci. USA 117, 14503–14511. 10.1073/pnas.1922563117. [PubMed: 32513712]

Groc L, and Choquet D (2020). Linking glutamate receptor movements and synapse function. Science 368, eaay4631. 10.1126/science.aay4631. [PubMed: 32527803]

Guthrie DA, Klein Herenbrink C, Lycas MD, Ku T, Bonifazi A, DeVree BT, Mathiasen S, Javitch JA, Grimm JB, Lavis L, et al. (2020). Novel fluorescent ligands enable single-molecule localization microscopy of the dopamine transporter. ACS Chem. Neurosci. 11, 3288–3300. 10.1021/acschemneuro.0c00397. [PubMed: 32926777]

Hamilton PJ, Belovich AN, Khelashvili G, Saunders C, Erreger K, Javitch JA, Sitte HH, Weinstein H, Matthies HJG, and Galli A (2014). PIP2 regulates psychostimulant behaviors through its interaction with a membrane protein. Nat. Chem. Biol. 10, 582–589. 10.1038/nchembio.1545. [PubMed: 24880859]

Hansen FH, Skjørringe T, Yasmeen S, Arends NV, Sahai MA, Erreger K, Andreassen TF, Holy M, Hamilton PJ, Neergheen V, et al. (2014). Missense dopamine transporter mutations associate with adult parkinsonism and ADHD. J. Clin. Invest. 124, 3107–3120. 10.1172/JCI73778. [PubMed: 24911152]

Herborg F, Andreassen TF, Berlin F, Loland CJ, and Gether U (2018). Neuropsychiatric disease-associated genetic variants of the dopamine transporter display heterogeneous molecular phenotypes. J. Biol. Chem. 293, 7250–7262. 10.1074/jbc.RA118.001753. [PubMed: 29559554]

Hong WC, and Amara SG (2010). Membrane cholesterol modulates the outward facing conformation of the dopamine transporter and alters cocaine binding. J. Biol. Chem. 285, 32616–32626. 10.1074/jbc.M110.150565. [PubMed: 20688912]

Hwang J, Tamm LK, Bohm C, Ramalingam TS, Betzig E, and Edidin M (1995). Nanoscale complexity of phospholipid monolayers investigated by near-field scanning optical microscopy. Science 270, 610–614. 10.1126/science.270.5236.610. [PubMed: 7570018]

Iversen LL (1975). Dopamine receptors in the brain. Science 188, 1084–1089. 10.1126/science.2976. [PubMed: 2976]

Jeong JY, Yim HS, Ryu JY, Lee HS, Lee JH, Seen DS, and Kang SG (2012). One-step sequence- and ligation-independent cloning as a rapid and versatile cloning method for functional genomics studies. Appl. Environ. Microbiol. 78, 5440–5443. 10.1128/AEM.00844-12. [PubMed: 22610439]

Kasture A, El-Kasaby A, Szöllősi D, Asjad HMM, Grimm A, Stockner T, Hummel T, Freissmuth M, and Sucic S (2016). Functional rescue of a misfolded Drosophila melanogaster dopamine transporter mutant associated with a sleepless phenotype by pharmacological chaperones. J. Biol. Chem. 291, 20876–20890. 10.1074/jbc.M116.737551. [PubMed: 27481941]

Klein Herenbrink C, Støier JF, Reith WD, Dagra A, Gregorek MAC, Cola RB, Patriarchi T, Li Y, Tian L, Gether U, and Herborg F (2022). Multimodal detection of dopamine by sniffer cells expressing genetically encoded fluorescent sensors. Commun. Biol. 5, 578. 10.1038/s42003-022-03488-5. [PubMed: 35689020]

Klewe IV, Nielsen SM, Tarpø L, Urizar E, Dipace C, Javitch JA, Gether U, Egebjerg J, and Christensen KV (2008). Recruitment of beta-arrestin2 to the dopamine D2 receptor: insights into anti-psychotic and antiparkinsonian drug receptor signaling. Neuropharmacology 54, 1215–1222. 10.1016/j.neuropharm.2008.03.015. [PubMed: 18455202]

Kristensen AS, Andersen J, Jørgensen TN, Sørensen L, Eriksen J, Loland CJ, Strømgaard K, and Gether U (2011). SLC6 neurotransmitter transporters: structure, function, and regulation. Pharmacol. Rev. 63, 585–640. 10.1124/pr.108.000869. [PubMed: 21752877]

Kuzhikandathil EV, Yu W, and Oxford GS (1998). Human dopamine D3 and D2L receptors couple to inward rectifier potassium channels in mammalian cell lines. Mol. Cell. Neurosci. 12, 390–402. 10.1006/mcne.998.0722. [PubMed: 9888991]

Lebowitz JJ, Pino JA, Mackie PM, Lin M, Hurst C, Divita K, Collins AT, Koutzoumis DN, Torres GE, and Khoshbouei H (2019). Clustered Kv2.1 decreases dopamine transporter activity and internalization. J. Biol. Chem. 294, 6957–6971. 10.1074/jbc.RA119.007441. [PubMed: 30824538]

Lee FJS, Pei L, Moszczynska A, Vukusic B, Fletcher PJ, and Liu F (2007). Dopamine transporter cell surface localization facilitated by a direct interaction with the dopamine D2 receptor. EMBO J. 26, 2127–2136. 10.1038/sj.emboj.7601656. [PubMed: 17380124]

Levet F, Julien G, Galland R, Butler C, Beghin A, Chazeau A, Hoess P, Ries J, Giannone G, and Sibarita JB (2019). A tessellation-based colocalization analysis approach for single-molecule

localization microscopy. Nat. Commun. 10, 2379. 10.1038/s41467-019-10007-4. [PubMed: 31147535]

Li Y, Mund M, Hoess P, Deschamps J, Matti U, Nijmeijer B, Sabinina VJ, Ellenberg J, Schoen I, and Ries J (2018). Real-time 3D single-molecule localization using experimental point spread functions. Nat. Methods 15, 367–369. 10.1038/nmeth.4661. [PubMed: 29630062]

Lin C-W, Sim S, Ainsworth A, Okada M, Kelsch W, and Lois C (2010). Genetically increased cell-intrinsic excitability enhances neuronal integration into adult brain circuits. Neuron 65, 32–39. 10.1016/j.neuron.2009.12.001. [PubMed: 20152111]

Liu C, and Kaeser PS (2019). Mechanisms and regulation of dopamine release. Curr. Opin. Neurobiol. 57, 46–53. 10.1016/j.conb.2019.01.001. [PubMed: 30769276]

Loland CJ, Desai RI, Zou MF, Cao J, Grundt P, Gerstbrein K, Sitte HH, Newman AH, Katz JL, and Gether U (2008). Relationship between conformational changes in the dopamine transporter and cocaine-like subjective effects of uptake inhibitors. Mol. Pharmacol. 73, 813–823. 10.1124/mol.107.039800. [PubMed: 17978168]

Loland CJ, Grånäs C, Javitch JA, and Gether U (2004). Identification of intracellular residues in the dopamine transporter critical for regulation of transporter conformation and cocaine binding. J. Biol. Chem. 279, 3228–3238. 10.1074/jbc.M304755200. [PubMed: 14597628]

Maidorn M, Olichon A, Rizzoli SO, and Opazo F (2019). Nanobodies reveal an extra-synaptic population of SNAP-25 and Syntaxin 1A in hippocampal neurons. mAbs 11, 305–321. 10.1080/19420862.2018.1551675. [PubMed: 30466346]

Maldonado R, Saiardi A, Valverde O, Samad TA, Roques BP, and Borrelli E (1997). Absence of opiate rewarding effects in mice lacking dopamine D2 receptors. Nature 388, 586–589. 10.1038/41567. [PubMed: 9252189]

Manley S, Gillette JM, Patterson GH, Shroff H, Hess HF, Betzig E, and Lippincott-Schwartz J (2008). High-density mapping of single-molecule trajectories with photoactivated localization microscopy. Nat. Methods 5, 155–157. 10.1038/nmeth.1176. [PubMed: 18193054]

Matsui R, Tanabe Y, and Watanabe D (2012). Avian adeno-associated virus vector efficiently transduces neurons in the embryonic and post-embryonic chicken brain. PLoS One 7, e48730. 10.1371/journal.pone.0048730. [PubMed: 23144948]

Maxfield FR, and McGraw TE (2004). Endocytic recycling. Nat. Rev. Mol. Cell Biol. 5, 121–132. 10.1038/nrm1315. [PubMed: 15040445]

McLaughlin S, and Murray D (2005). Plasma membrane phosphoinositide organization by protein electrostatics. Nature 438, 605–611. 10.1038/nature04398. [PubMed: 16319880]

Meiergerd SM, Patterson TA, and Schenk JO (1993). D2 receptors may modulate the function of the striatal transporter for dopamine: kinetic evidence from studies in vitro and in vivo. J. Neurochem. 61, 764–767. 10.1111/j.1471-4159.1993.tb02185.x. [PubMed: 8336153]

Newman AH, Cao J, Keighron JD, Jordan CJ, Bi GH, Liang Y, Abramyan AM, Avelar AJ, Tschumi CW, Beckstead MJ, et al. (2019). Translating the atypical dopamine uptake inhibitor hypothesis toward therapeutics for treatment of psychostimulant use disorders. Neuropsychopharmacology 44, 1435–1444. 10.1038/s41386-019-0366-z. [PubMed: 30858517]

Ovesný M, Křížek P, Borkovec J, Svindrych Z, and Hagen GM (2014). ThunderSTORM: a comprehensive ImageJ plug-in for PALM and STORM data analysis and super-resolution imaging. Bioinformatics 30, 2389–2390. 10.1093/bioinformatics/btu202. [PubMed: 24771516]

Padmanabhan P, Bademosi AT, Kasula R, Lauwers E, Verstreken P, and Meunier FA (2020). Need for speed: super-resolving the dynamic nanoclustering of syntaxin-1 at exocytic fusion sites. Neuropharmacology 169, 107554. 10.1016/j.neuropharm.2019.02.036. [PubMed: 30826343]

Parsons LH, Schad CA, and Justice JB (1993). Coadministration of the d2 antagonist pimozide inhibits up-regulation of dopamine release and uptake induced by repeated cocaine. J. Neurochem. 60, 376–379. 10.1111/j.1471-4159.1993.tb05864.x. [PubMed: 8417161]

Pereira DB, Schmitz Y, Mészáros J, Merchant P, Hu G, Li S, Henke A, Lizardi-Ortiz JE, Karpowicz RJ Jr., Morgenstern TJ, et al. (2016). Fluorescent false neurotransmitter reveals functionally silent dopamine vesicle clusters in the striatum. Nat. Neurosci. 19, 578–586. 10.1038/nn.4252. [PubMed: 26900925]

Piedra J, Ontiveros M, Miravet S, Penalva C, Monfar M, and Chillon M (2015). Development of a rapid, robust, and universal picogreen-based method to titer adeno-associated vectors. Hum Gene Ther Methods 26, 35–42. 10.1089/hgtb.2014.120. [PubMed: 25640021]

Prasad BM, and Amara SG (2001). The dopamine transporter in mesencephalic cultures is refractory to physiological changes in membrane voltage. J. Neurosci. 21, 7561–7567. [PubMed: 11567046]

Qi Y, Wang JK, McMillian M, and Chikaraishi DM (1997). Characterization of a CNS cell line, CAD, in which morphological differentiation is initiated by serum deprivation. J. Neurosci. 17, 1217–1225. [PubMed: 9006967]

Rahbek-Clemmensen T, Lycas MD, Erlendsson S, Eriksen J, Apuschkin M, Vilhardt F, Jørgensen TN, Hansen FH, and Gether U (2017). Super-resolution microscopy reveals functional organization of dopamine transporters into cholesterol and neuronal activity-dependent nanodomains. Nat. Commun. 8, 740. 10.1038/s41467-017-00790-3. [PubMed: 28963530]

Ramamoorthy S, Shippenberg TS, and Jayanthi LD (2011). Regulation of monoamine transporters: role of transporter phosphorylation. Pharmacol. Ther. 129, 220–238. 10.1016/j.pharmthera.2010.09.009. [PubMed: 20951731]

Rayport S, Sulzer D, Shi WX, Sawasdikosol S, Monaco J, Batson D, and Rajendran G (1992). Identified postnatal mesolimbic dopamine neurons in culture: morphology and electrophysiology. J. Neurosci. 12, 4264–4280. [PubMed: 1359033]

Robertson SD, Matthies HJG, and Galli A (2009). A closer look at amphetamine-induced reverse transport and trafficking of the dopamine and norepinephrine transporters. Mol. Neurobiol. 39, 73–80. 10.1007/s12035-009-8053-4. [PubMed: 19199083]

Salamone A, Zappettini S, Grilli M, Olivero G, Agostinho P, Tomé AR, Chen J, Pittaluga A, Cunha RA, and Marchi M (2014). Prolonged nicotine exposure down-regulates presynaptic NMDA receptors in dopaminergic terminals of the rat nucleus accumbens. Neuropharmacology 79, 488–497. 10.1016/j.neuropharm.2013.12.014. [PubMed: 24373903]

Shivanandan A, Deschout H, Scarselli M, and Radenovic A (2014). Challenges in quantitative single molecule localization microscopy. FEBS Lett. 588, 3595–3602. 10.1016/j.febslet.2014.06.014. [PubMed: 24928440]

Siddig S, Aufmkolk S, Doose S, Jobin M-L, Werner C, Sauer M, and Calebiro D (2020). Super-resolution imaging reveals the nanoscale organization of metabotropic glutamate receptors at presynaptic active zones. Sci. Adv. 6, eaay7193. 10.1126/sciadv.aay7193. [PubMed: 32494600]

Sorkina T, Richards TL, Rao A, Zahniser NR, and Sorkin A (2009). Negative regulation of dopamine transporter endocytosis by membrane-proximal N-terminal residues. J. Neurosci. 29, 1361–1374. 10.1523/JNEUROSCI.3250-08.2009. [PubMed: 19193883]

Spyraki C, and Fibiger HC (1981). Intravenous self-administration of nomifensine in rats: implications for abuse potential in humans. Science 212, 1167–1168. 10.1126/science.7195072. [PubMed: 7195072]

Strange PG (2008). Antipsychotic drug action: antagonism, inverse agonism or partial agonism. Trends Pharmacol. Sci. 29, 314–321. 10.1016/j.tips.2008.03.009. [PubMed: 18471899]

Thal LB, Tomlinson ID, Quinlan MA, Kovtun O, Blakely RD, and Rosenthal SJ (2019). Single quantum dot imaging reveals PKCbeta-dependent alterations in membrane diffusion and clustering of an attention-deficit hyperactivity disorder/autism/bipolar disorder-associated dopamine transporter variant. ACS Chem. Neurosci. 10, 460–471. 10.1021/acschemneuro.8b00350. [PubMed: 30153408]

Torres GE (2006). The dopamine transporter proteome. J. Neurochem. 97 (Suppl 1), 3–10. 10.1111/j.1471-4159.2006.03719.x. [PubMed: 16635244]

Torres GE, and Amara SG (2007). Glutamate and monoamine transporters: new visions of form and function. Curr. Opin. Neurobiol. 17, 304–312. 10.1016/j.conb.2007.05.002. [PubMed: 17509873]

Tritsch NX, and Sabatini BL (2012). Dopaminergic modulation of synaptic transmission in cortex and striatum. Neuron 76, 33–50. 10.1016/j.neuron.2012.09.023. [PubMed: 23040805]

Truckenbrodt S, Sommer C, Rizzoli SO, and Danzl JG (2019). A practical guide to optimization in X10 expansion microscopy. Nat. Protoc. 14, 832–863. 10.1038/s41596-018-0117-3. [PubMed: 30778205]

Truckenbrodt S, Viplav A, Jähne S, Vogts A, Denker A, Wildhagen H, Fornasiero EF, and Rizzoli SO (2018). Newly produced synaptic vesicle proteins are preferentially used in synaptic transmission. EMBO J. 37, e98044. 10.15252/embj.201798044. [PubMed: 29950309]

Turkowyd B, Schreiber S, Wörtz J, Segal ES, Mevarech M, Duggin IG, Marchfelder A, and Endesfelder U (2020). Establishing live-cell single-molecule localization microscopy imaging and single-particle tracking in the archaeon haloferax volcanii. Front. Microbiol. 11, 583010. 10.3389/fmicb.2020.583010. [PubMed: 33329447]

Turner TJ, Adams ME, and Dunlap K (1993). Multiple Ca2+ channel types coexist to regulate synaptosomal neurotransmitter release. Proc. Natl. Acad. Sci. USA 90, 9518–9522. 10.1073/pnas.90.20.9518. [PubMed: 8415733]

Underhill SM, Wheeler DS, Li M, Watts SD, Ingram SL, and Amara SG (2014). Amphetamine modulates excitatory neurotransmission through endocytosis of the glutamate transporter EAAT3 in dopamine neurons. Neuron 83, 404–416. 10.1016/j.neuron.2014.05.043. [PubMed: 25033183]

van den Bogaart G, Meyenberg K, Risselada HJ, Amin H, Willig KI, Hubrich BE, Dier M, Hell SW, Grubmüller H, Diederichsen U, and Jahn R (2011). Membrane protein sequestering by ionic protein-lipid interactions. Nature 479, 552–555. 10.1038/nature10545. [PubMed: 22020284]

Wang Y, Schnitzbauer J, Hu Z, Li X, Cheng Y, Huang ZL, and Huang B (2014). Localization events-based sample drift correction for localization microscopy with redundant cross-correlation algorithm. Opt Express 22, 15982–15991. 10.1364/OE.22.015982. [PubMed: 24977854]

Xue M, Atallah BV, and Scanziani M (2014). Equalizing excitation-inhibition ratios across visual cortical neurons. Nature 511, 596–600. 10.1038/nature13321. [PubMed: 25043046]

Zapata A, Kivell B, Han Y, Javitch JA, Bolan EA, Kuraguntla D, Jaligam V, Oz M, Jayanthi LD, Samuvel DJ, et al. (2007). Regulation of dopamine transporter function and cell surface expression by D3 dopamine receptors. J. Biol. Chem. 282, 35842–35854. 10.1074/jbc.M611758200. [PubMed: 17923483]

Highlights

- The dopamine transporter (DAT) is localized to PIP2-enriched nanodomains
- Nanoclustered DAT is inward facing, and unclustered DAT is outward facing
- Excitatory input disperses DAT from nanodomains in a Ca^{2+}-dependent manner
- In contrast, dopamine D2 receptor activity promotes DAT nanodomain localization

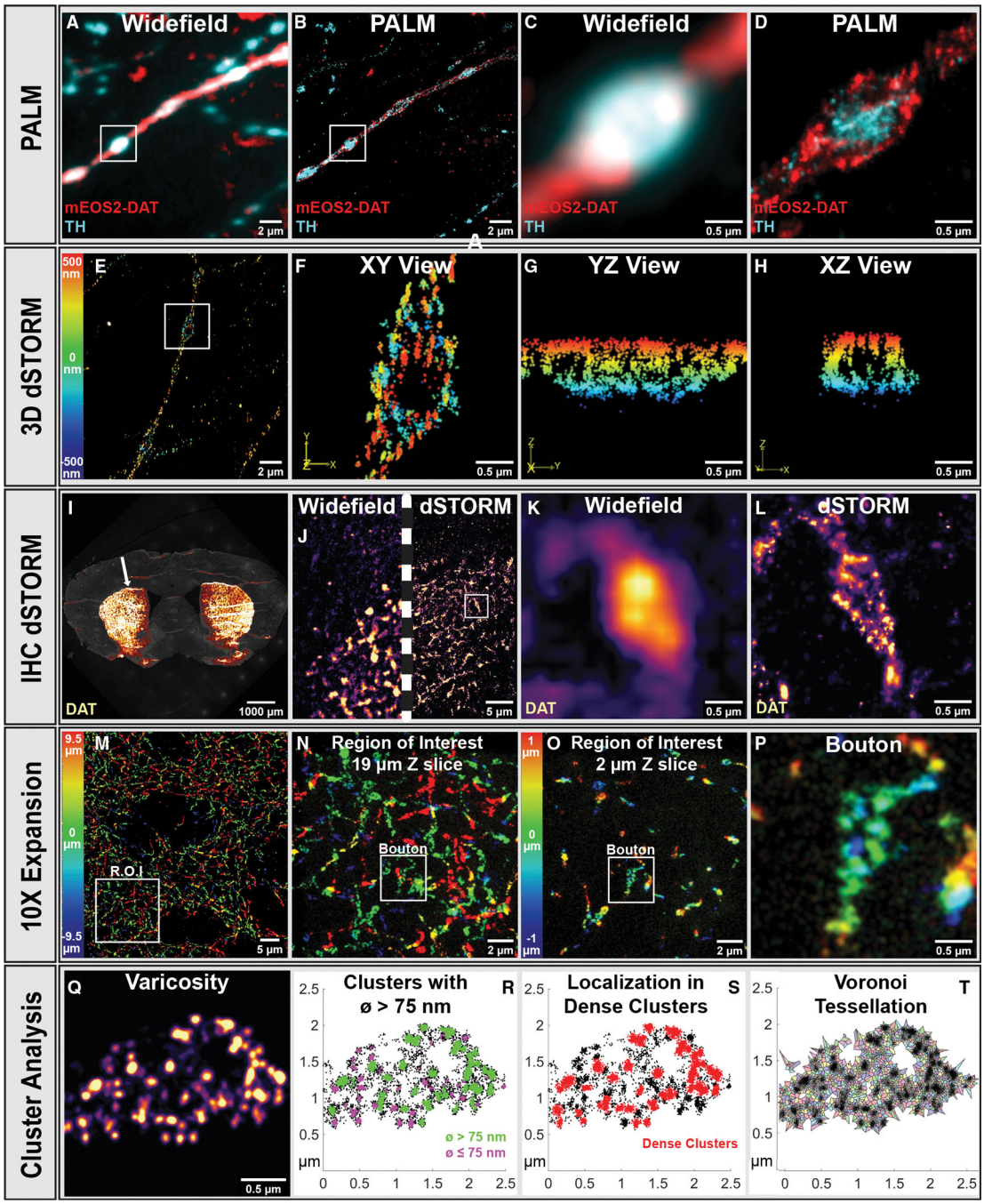

Figure 1. DAT shows nanodomain distribution in cultured neurons and striatal slices

(A–D) Visualization of mEos2-DAT in cultured DA neurons by PALM. Endogenous TH was labeled to identify DA neurons.

(A and C) Wide-field images (C shows the boxed region in A).

(B and D) PALM/dSTORM images (D shows the boxed region in B).

(E–H) 3D dSTORM image of DAT in DA neurons (color-coded based on depth).

(E) Neuronal extension.

(F) Varicosity (boxed region in E) (xy perspective).

(G) yz perspective.
(H) xz perspective.
(I–L) Mouse brain coronal section immunolabeled for DAT.
(I) Brain slice with striatal DAT staining.
(J) Comparison of wide field with dSTORM.
(K) Wide-field view of varicosity.
(L) dSTORM image.
(M–P) 10× expansion microscopy (ExM) on mouse striatal slice immunolabeled for DAT.
(N) The region of interest (ROI) in (M) with the full 19-μm z slice (color-coded based on depth).
(O) The ROI in (M) with just 2 μm of the z axis.
(P) Single varicosity identified in (O).
(Q–T) Cluster metrics demonstrated on a varicosity immunolabeled for DAT.
(Q) dSTORM of a single varicosity.
(R and S) Identification of clusters by DBSCAN. Green, clusters with a diameter greater than 75 nm; magenta, clusters smaller than 75 nm; red, dense clusters (>80 localizations within a radius of 50 nm).
(T) DAT localizations segmented by Voronoi tessellation.
See also Figures S1 and S2.

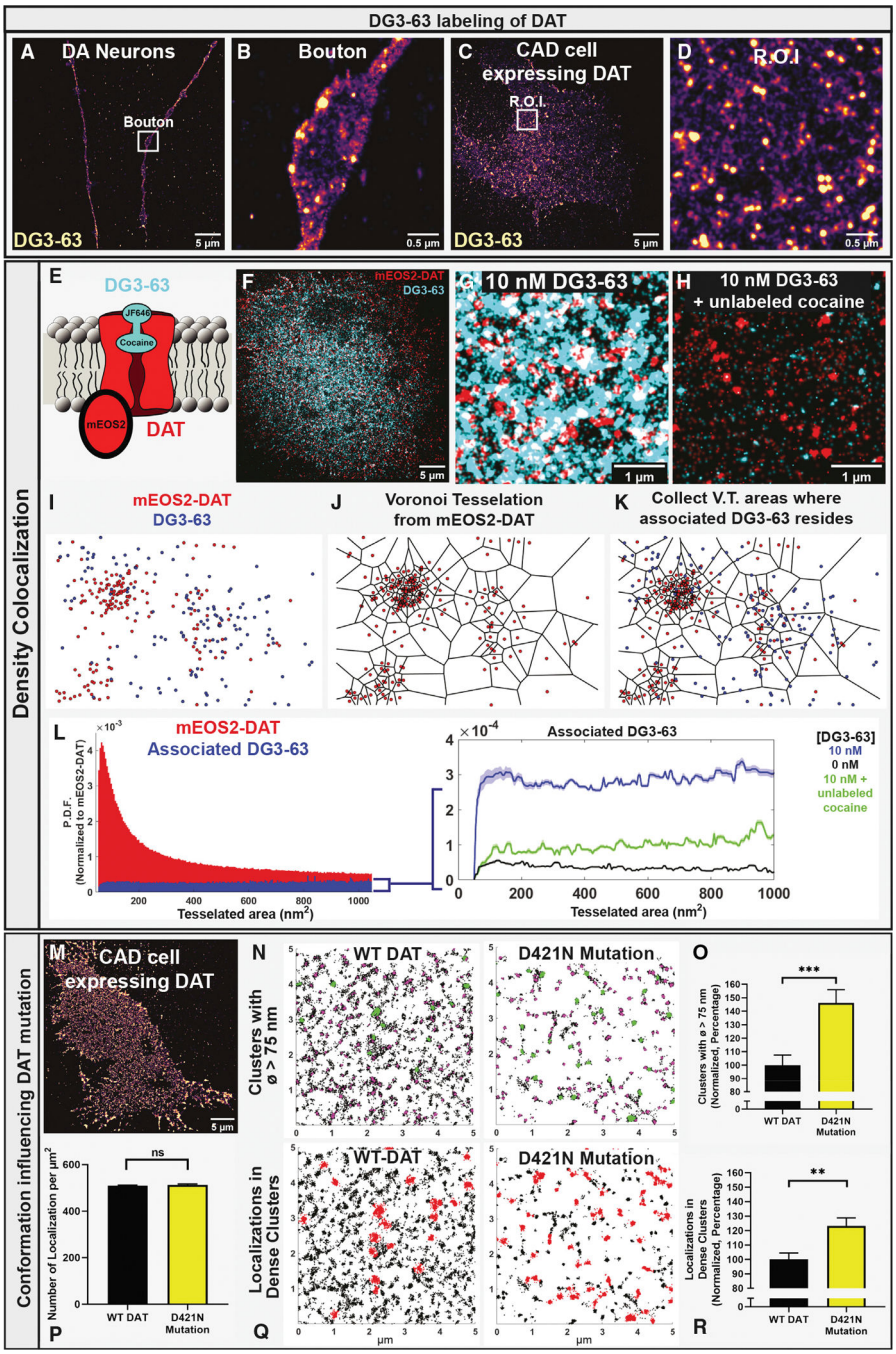

Figure 2. Nanodomain-localized DAT is preferentially in an inward-facing conformation

(A–D) dSTORM on DA neurons and DAT-expressing CAD cells labeled with the fluorescent cocaine analog DG3–63 (10 nM).

(A) Axonal extension.

(B) Varicosity (box in A).

(C) CAD cell.

(D) ROI from (C).

(E–H) The density-based association of DG3–63 with mEOS2-DAT.

(E) Cartoon of the labeling strategy.
(F) dSTORM/PALM image of a CAD cell expressing mEOS2-DAT (red) and labeled with DG3–63 (10 nM) (blue).
(G) Close up dSTORM/PALM image of CAD cell expressing mEOS2-DAT (red) and labeled with DG3–63 (10 nM) (blue).
(H) The DG3–63 signal is blocked by 100 μM cocaine.
(I–L) Voronoi tessellation-based colocalization algorithm. Tessellation is performed on the mEOS2-DAT data, and areas are marked when the mEOS2-DAT localization has a DG3–63 localization within 25 nm.
(L) Left: total mEos2-DAT Voronoi tesselated area distribution (red) (probability density function [PDF]) and tessellated areas of mEos2-DAT associated with DG3–63 (blue). Right: tessellated areas for mEos2-DAT associated with DG3–63 (blue) compared with that associated in the presence of saturating cocaine.
(M–O) Total internal reflection fluorescence (TIRF)/dSTORM of WT DAT and the inward-facing mutant (D421N) expressed in CAD cells.
(M) Example image of DAT expressed in CAD cells.
(N) Example images of DAT clusters identified by DBSCAN in WT DAT and D421N D expressing cells; clusters with diameter >75 nm in green, clusters <75 nm in magenta.
(O) Normalized fraction of clusters with a diameter greater than 75 nm (percent). Means ± S.E. from 38 WT DAT cells and 42 D421N cells, 3 transfections, ***$p < 0.001$, unpaired t test.
(P–R) dSTORM of WT DAT and the inward-facing mutant (D421N) expressed in CAD cells.
(P) Number of localizations per square meter for WT DAT and D421N. Means ± S.E., unpaired t test, $p = 0.4$.
(Q) Example images of DAT clusters identified by DBSCAN in WT DAT and D421N D expressing cells; dense clusters (>80 localizations within a radius of 50 nm) in red.
(R) Fraction of localizations in dense clusters (in percent of WT DAT). Means ± S.E. from 38 WT DAT cells and 42 D421N cells, 3 transfections, **$p < 0.01$, unpaired t test.
See also Figure S3.

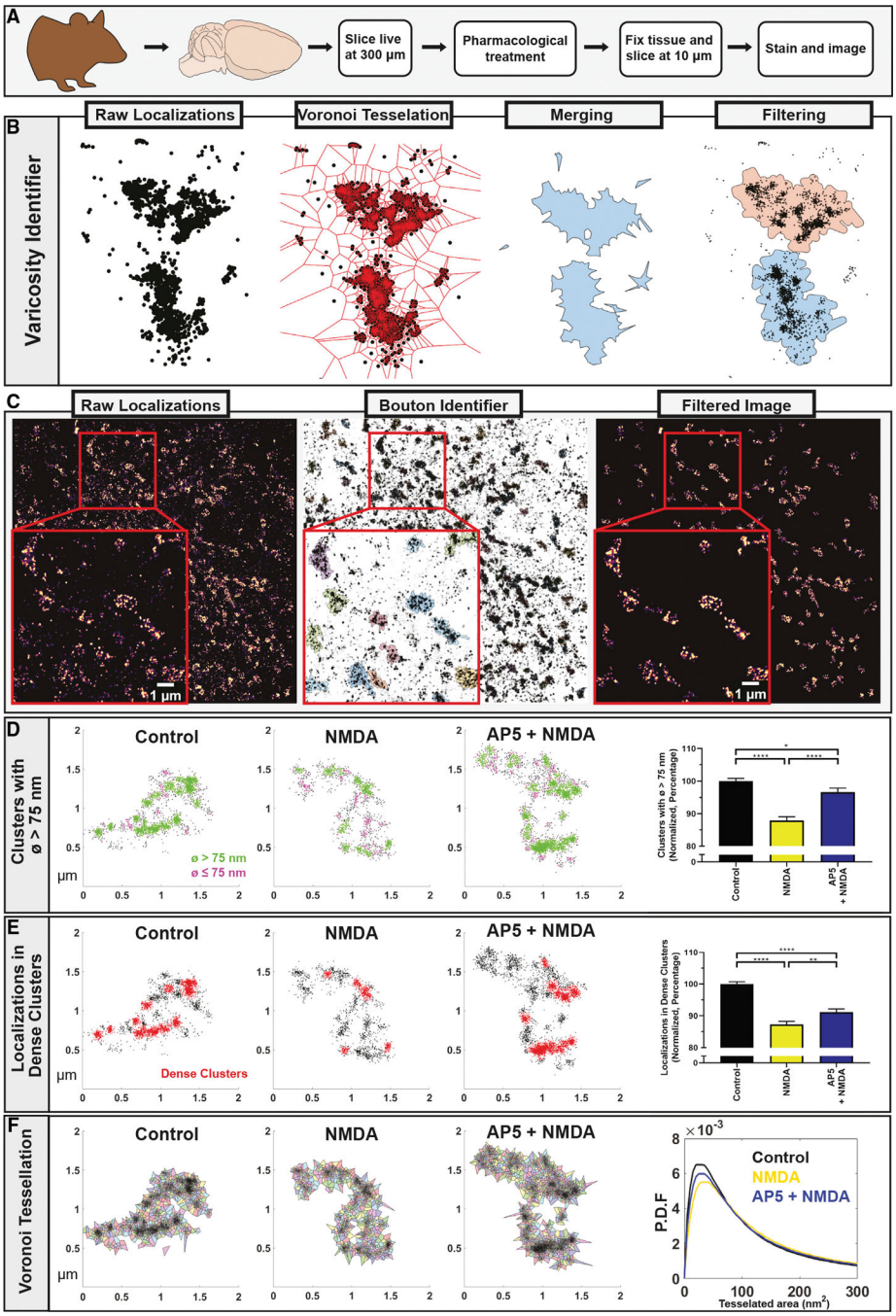

Figure 3. NMDA receptor activation declusters DAT in mouse brain slices

(A) Workflow diagram.

(B) Data processing steps to isolate single varicosities from dSTORM images.

(C) Representative DAT dSTORM image before, during, and after varicosity identification.

(D) Example varicosity from control, NMDA-, and AP5 plus NMDA-treated slices (clusters with diameter >75 nm in green, clusters < 75 nm in magenta). Right: normalized fraction of DAT clusters greater than 75 nm (percent). Means ± S.E. from 3 experiments with analysis

of 1,793 control, 1,102 NMDA, and 1,033 NMDA plus AP5 varicosities; one-way ANOVA, ****$p < 0.0001$, *$p < 0.05$.

(E) Example varicosity from control, NMDA (20 μM)-, and AP5 plus NMDA (20 μM)-treated slices (dense clusters in red, >80 localizations; radius, 50 nm). Right: normalized fraction of DAT localizations in dense clusters (percent). Means ± S.E.; one-way ANOVA, ****$p < 0.0001$, ***$p < 0.001$, **$p < 0.01$.

(F) The PDFs for the Voronoi tessellated areas, averaged by varicosity.

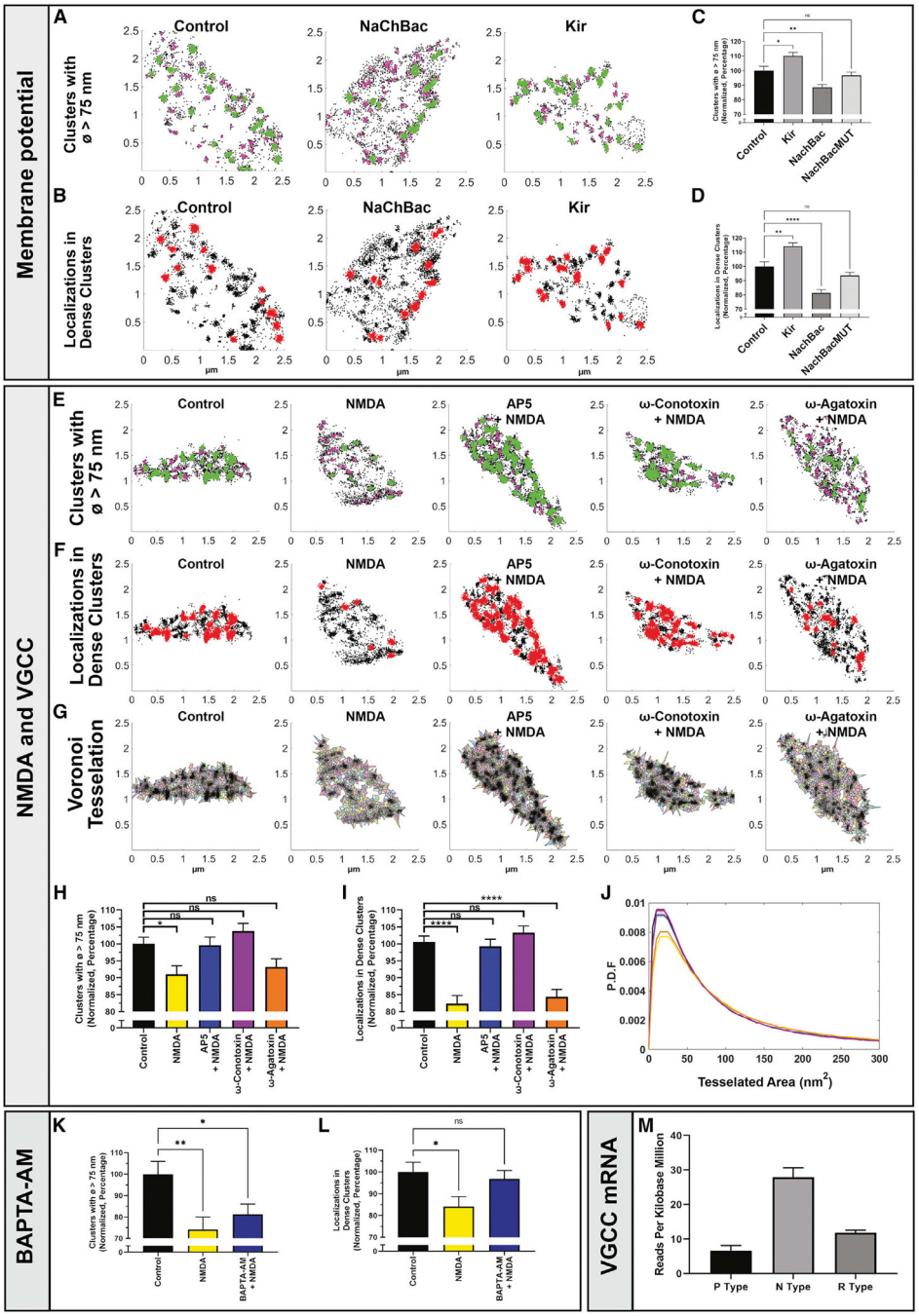

Figure 4. DAT nanodomain localization is regulated by neuronal activity in a Ca^{2+}-dependent manner

(A–D) Expression of the Na^+ channel mNaChBac or the K^+ channel Kir2.1 in DA neurons. Shown are example varicosities from DAT dSTORM of control, mNaChBac-, or Kir2.1-expressing DA neurons.

(A) DAT clusters with a diameter greater than 75 nm are shown in green and clusters smaller than 75 nm in magenta.

(B) Dense DAT clusters are shown in red (>80 localizations; radius, 50 nm).

(C) Normalized fraction of clusters greater than 75 nm (percent).

(D) Normalized fraction of DAT localizations in dense clusters (percent. Means ± S.E.; data from 3 cultures and 128 control, 290 mNaChBac, 220 Kir2.1, and 211 mNaChBac MUT varicosities; one-way ANOVA, ****p < 0.0001, **p < 0.01, *p < 0.05; n.s., not significant.
(E–J) The effect of NMDA on DAT nanodomains is blocked by the N-type VGCC blocker ω-conotoxin. Shown are example varicosities from dSTORM of DA neurons subject to 5-min treatment with vehicle, NMDA (20 μM), AP5 (100 μM) plus NMDA (20 μM), ω-conotoxin (1 μM) plus NMDA (20 μM), or ω-agatoxin (1 μM) plus NMDA (20 μM).
(E) DAT clusters with a diameter greater than 75 nm are shown in green and clusters smaller than 75 nm in magenta.
(F) Dense DAT clusters are shown in red (>80 localizations; radius, 50 nm).
(G) Localizations segmented by Voronoi tessellation.
(H and I) Normalized fraction of DAT clusters greater than 75 nm (percent) (H) and normalized fraction of DAT localizations in dense clusters (percent) (I). Means ± S.E.; one-way ANOVA, ****p< <0.0001, *p < 0.05.
(J) PDFs (curves are color coded as in the bar diagrams) for the Voronoi tessellated areas averaged by varicosity. Data are from 3 cultures and 190 control, 147 NMDA, 170 AP5, 180 ω-conotoxin, and 154 ω-agatoxin varicosities.
(K and L) Pretreatment (30 min) with BAPTA-AM inhibits the dispersing effect of NMDA on DAT nanodomains.
(K and L) Normalized fraction of DAT clusters greater than 75 nm (percent) (K) and normalized fraction of DAT localizations in dense clusters (percent) (L) for control, NMDA (20 μM) and NMDA (20 μM) plus BAPTA-AM (25 μM). Means ± S.E.; data are from 3 cultures and include analysis of 66 control, 72 NMDA, and 70 BAPTA-AM plus NMDA varicosities; one-way ANOVA, **p < 0.01, *p < 0.05.
(M) mRNA expression for P-, R-, and N-type VGCCs in DA neurons based on single-cell RNA sequencing (RNA-seq) data. Data are means ± SE of five data sets (STAR Methods). See also Figure S4 and Videos S1 and S2.

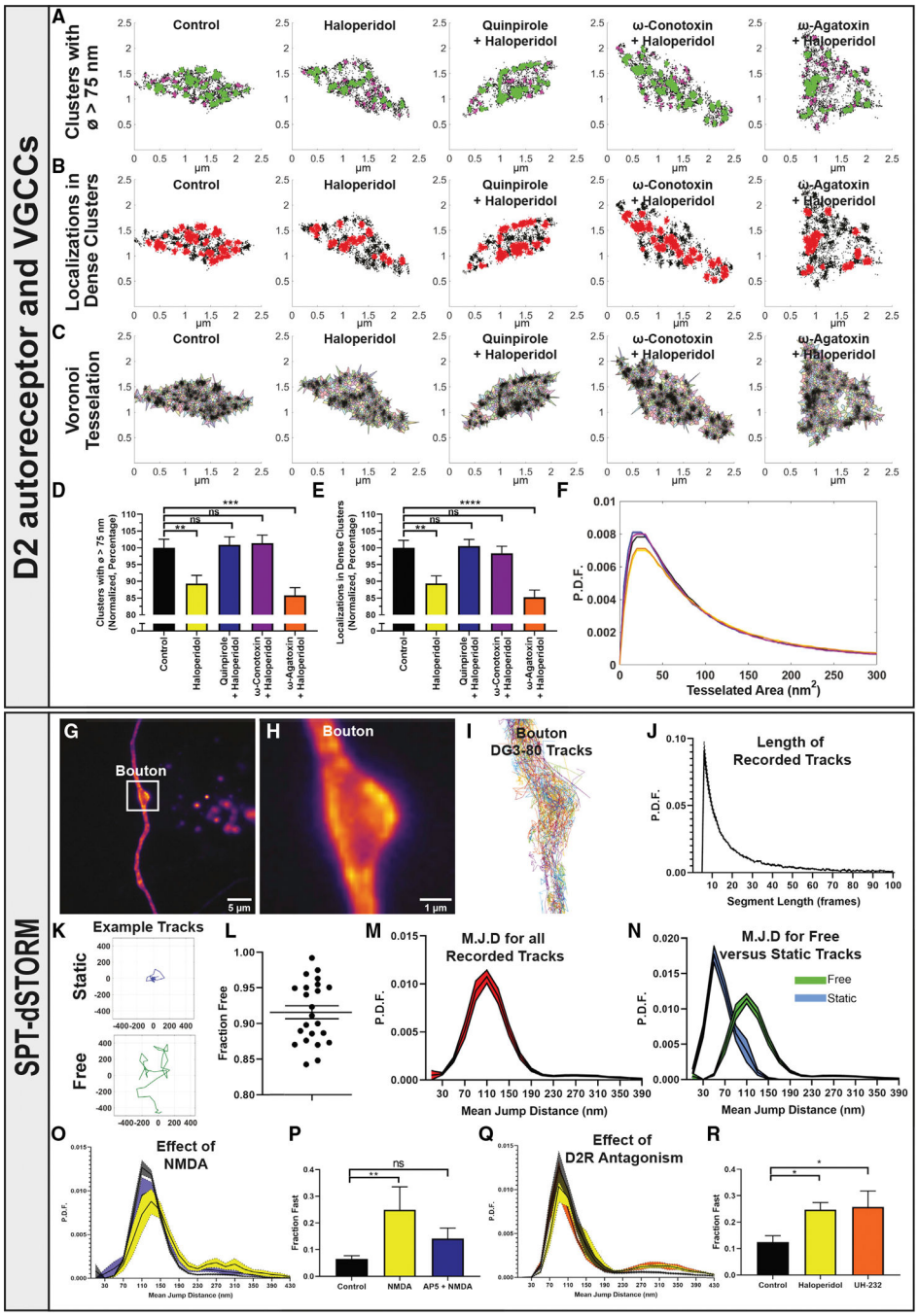

Figure 5. DAT nanodomain localization is regulated by the D2R and involves changes in lateral mobility

(A–F) Dispersal of DAT nanodomains is promoted by the D2R antagonist haloperidol and blocked by the agonist quinpirole and by the N-type VGCC blocker ω-conotoxin. Shown are example varicosities from dSTORM of DA neurons subjected to 5-min treatment with haloperidol (10 nM), haloperidol (10 nM) plus quinpirole (50 μM), haloperidol (10 nM) plus ω-conotoxin (1 μM), or haloperidol (10 nM) plus ω-agatoxin (1 μM).

(A) DAT clusters with a diameter greater than 75 nm are shown in green and clusters smaller than 75 nm in magenta.

(B) Dense DAT clusters are shown in red (>80 localizations; radius, 50 nm).
(C) Localizations segmented by Voronoi tessellation.
(D and E) Normalized fraction of DAT clusters greater than 75 nm (percent) (D) and normalized fraction of DAT localizations in dense clusters (percent) (E). Means ± S.E.; one-way ANOVA, ****$p < 0.0001$, ***$p < 0.001$, **$p < 0.01$, *$p < 0.05$.
(F) PDFs (curves are color coded as in the bar diagrams) for the Voronoi tessellated areas averaged by varicosity. Data are from 3 cultures and 153 control, 166 haloperidol, 167 quinpirole, 178 ω-conotoxin, and 176 ω-agatoxin varicosities.
(G–R) Single-particle tracking dSTORM (SPT-dSTORM) identifies changes in DAT mobility in response to NMDA and D2R antagonism.
(G) Example live dSTORM images of DA neurons labeled with the fluorescent cocaine analog DG3–80.
(H) Boxed region in (B).
(I and J) Detected tracks (I) and distribution of segment lengths (J) in a varicosity from the control SPT-dSTORM experiment (16-ms frame rate).
(K) Example traces of a confined and an unconstrained freely moving particle (DG3–80-labeled DAT).
(L) Fraction of unconstrained tracks of the total number of tracks. Data are means of 23 tracks ± S.E.
(M) PDF for total mean jump distances (MJD) (i.e., the distance an individual molecule/particle has traveled between each image) for control experiments.
(N) PDF when separated into static and freely moving particles. Among the freely moving particles, some moved very fast with MJDs of 200–350 nm.
(O) NMDA (20 μM, 5 min) increases the population of DAT molecules with MJDs greater than 200 nm, which is blunted by AP5 (100 μM).
(P) Fraction of fast-moving particles (>200 nm). Means ± S.E.; data from 13 control, 4 NMDA, and 5 NMDA plus AP5 experiments.
(Q) The D2R antagonists haloperidol (10 nM, 5 min) and UH-232 (1 μM) increase the population of DAT molecules with MJDs greater than 200 nm.
(R) fraction of fast-moving particles (>200 nm), Means ± S.E.; data are from 10 control, 6 haloperidol, and 5 UH-232 experiments; one-way ANOVA, *$p < 0.05$; **$p < 0.01$.
See also Figure S5, Videos S1 and S3.

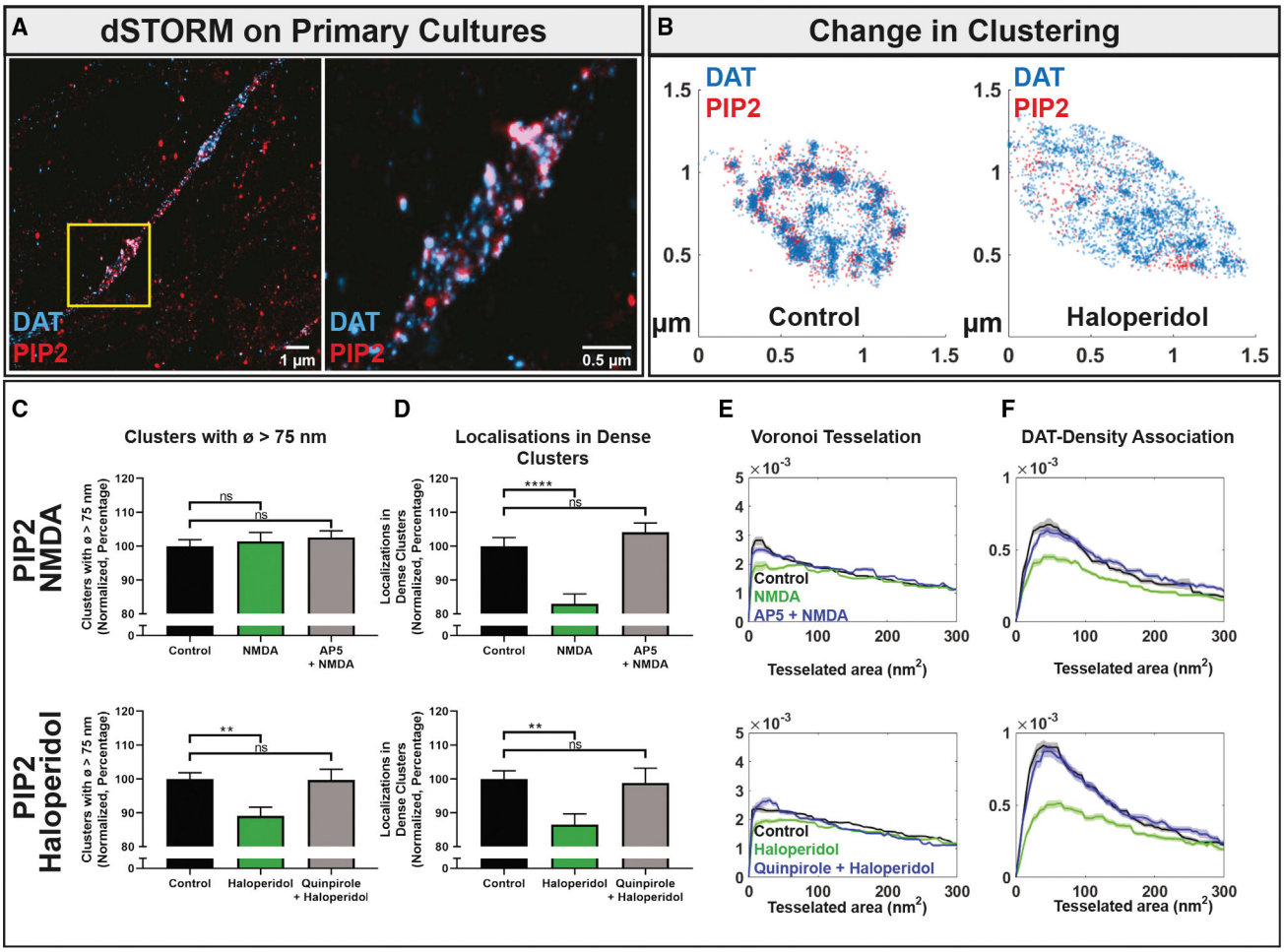

Figure 6. DAT nanodomains overlap with PIP2 nanodomains

(A) Example dual-color dSTORM images of phosphatidylinositol 4,5-bisphosphate (PIP2) (red, CF568) and DAT (blue, Alexa 647) in a neuronal extension from cultured DA neurons (left), with a close-up image of varicosity (right) corresponding to the boxed region in the left image.

(B) Example dual-color dSTORM images of varicosities from DA neurons showing localizations for PIP2 (red) and DAT (blue). Left: control. right: neurons exposed to haloperidol (10 nM, 5 min).

(C–F) Effect of NMDA and haloperidol on PIP2 clustering. Top panels: control, NMDA (20 µM), and NMDA (20 µM) plus AP5 (100 µM). Bottom panels: control, haloperidol (10 nM), and haloperidol (10 nM) plus quinpirole (50 µM).

(C and D) Normalized fraction of PIP2 localizations in large clusters (>75 nm in diameter) (percent) (C) and normalized fraction of PIP2 localizations in dense clusters (>80 localizations; radius, 50 nm) (percent) (D). Means ± S.E., one-way ANOVA, ****$p < 0.0001$, **$p < 0.01$.

(E) PDFs (color-coded as in the bar diagrams) for the Voronoi tessellated areas averaged by varicosity.

(F) PDFs (color-coded as in the bar diagrams) of the association of PIP2 with DAT clusters determined by Voronoi tessellation-based association (Figure 2), showing strong association

of PIP2 with DAT. Data are from 3 cultures and 137 control, 126 NMDA, and 121 NMDA plus AP5 varicosities and 140 control, 102 haloperidol, and 67 haloperidol plus quinpirole varicosities.

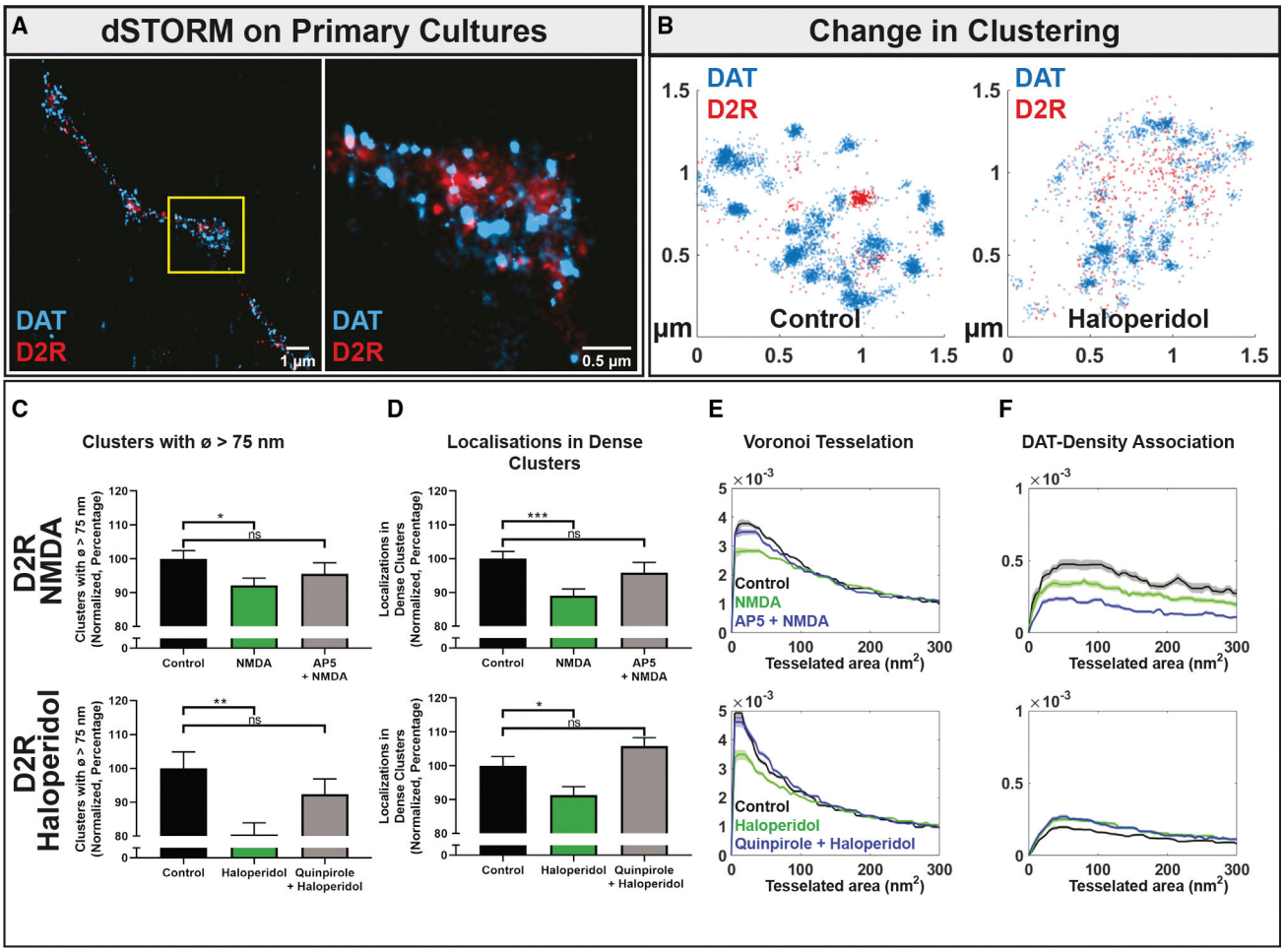

Figure 7. The D2R is also distributed into nanodomains

(A) Example dual-color dSTORM images of the D2R (red, CF568) and DAT (blue, Alexa 647) in a DA neuronal extension (left) with a close-up image of a varicosity (right) corresponding to the boxed region in the left image.

(B) Example dual-color dSTORM images of varicosities from DA neurons showing localizations for D2R (red) and DAT (blue). Left: control. Right: neurons exposed to haloperidol (10 nM, 5 min).

(C–F) Effect of NMDA and haloperidol on D2R clustering. Top panels: control, NMDA (20 µM), and NMDA (20 µM) plus AP5 (100 µM). Bottom panels: control, haloperidol (10 nM), and haloperidol (10 nM) plus quinpirole (50 µM).

(C and D) Normalized fraction of D2R localizations in large clusters (>75 nm in diameter) (percent) (C) and normalized fraction of D2R localizations in dense clusters (>80 localizations; radius, 50 nm) (percent). Means ± S.E., one-way ANOVA, ***$p < 0.001$, **$p < 0.01$, *$p < 0.05$.

(E) PDFs (color-coded as in the bar diagrams) for the Voronoi tessellated areas averaged by varicosity.

(F) PDFs (color-coded as in the bar diagrams) of the association of D2R with DAT clusters determined by Voronoi tessellation-based association (Figure 2). Data are from 3 cultures

and 112 control, 157 NMDA, and 75 NMDA plus AP5 varicosities and 179 control, 195 haloperidol, and 150 quinpirole varicosities.
See also Figures S5 and S6.

KEY RESOURCES TABLE

REAGENT or RESOURCE	SOURCE	IDENTIFIER
Antibodies		
Rat Anti-DAT	Millipore	MAB369 RRID:AB_2190413
Mouse Anti-TH	Millipore	MAB318 RRID:AB_2201528
Rabbit Anti-tRFP	Evrogen	AB233 RRID:AB_2571743
Rabbit Anti-D2R	Synaptic Systems	376 203 RRID:AB_2636918
Mouse Anti-STX1	Synaptic Systems	110 011 RRID:AB_887844
Mouse Anti-PIP2	Abcam	Ab11039 RRID:AB_442848
Mouse Anti-Clathrin light chain	Synaptic Systems	113 011 RRID:AB_887706
Donkey Anti-Rat	Jackson	712-005-153 RRID:AB_2340631
Donkey Anti-Mouse	Jackson	715-005-151 RRID:AB_2340759
Donkey Anti-Rabbit	Jackson	711-005-152 RRID:AB_2340585
Mouse Anti-synaptotagmin 1	Synaptic systems	105 311 RRID:AB_10805653
Bacterial and virus strains		
pAAV-CAG-Flex-NES-jRGECO1a-WPREpA	Addgene	RRID: Addgene #100854
pAAV-pTH-iCre-WPREpA	This paper	N/A
pAAV-hSyn-DIO-mNaChBac-T2A-mKate2-WPREpA	This paper	Adapted from RRID: Addgene #60658
pAAV-hSyn-DIO-mNaChBac-MUT- T2A-mKate2-WPREpA	This paper	Adapted from RRID: Addgene #60658
pAAV-hSyn-DIO-Kir2.1-T2A-mKate2-WPREpA	This paper	Adapted from RRID: Addgene #60661
Chemicals, peptides, and recombinant proteins		
Alexa647 NHS ester	ThermoFisher	A20006
CF568 NHS ester	Biotum	92131
NMDA (N-methyl-D-aspartate)	Sigma	M3262
DL-AP5	Tocris	0105
omega-conotoxin GVIA	Abcam	Ab120215
omega-agatoxin IVA	Abcam	ab120210
Quinpirole	Sigma-Aldrich	Q102
Haloperidol	Sigma-Aldrich	H1512
Nomifensine	Tocris Bioscience	1992
Cocaine	Sigma-Aldrich	C5776
JHW007	Synthesized by Amy Newman	N/A
Noribogaine	Gift from Sacrament of Transition (Maribor, Slovenia)	N/A
Dopamine	Sigma-Aldrich	H8502
UH-232	Tocris	0775
DG3-63	Guthrie et al., 2020	N/A
DG3-80	Guthrie et al., 2020	N/A

REAGENT or RESOURCE	SOURCE	IDENTIFIER
NeuroMag reagent	OZ biosciences	NM50200
Experimental models: Cell lines		
Cath.a-differentiated (CAD) cells (Qi et al., 1997)	Sigma	08100805
HEK cells (human embryonic kidney cells)	ATCC	ATCC CRL-1573
Rat primary midbrain dopaminergic cultures from pups of Wistar IGS rats	This paper	N/A
Experimental models: Organisms/strains		
Timed pregnancy, day 15, Wistar IGS rats	Scanbur (Charles River)	94-003-WI-F-TP15
C57BL/6J mice	Scanbur (Charles River)	000664
Recombinant DNA		
pmEOS2-hDAT	This paper	Generated from pmEOS2-C1 (RRID: Addgene #54510)
pRC/CMV hDAT	Herborg et al., 2018	N/A
pRC/CMV hDAT D421N	Herborg et al., 2018	N/A
pcDNA 3.1-SF-D2s	Klewe et al., 2008	N/A
Software and algorithms		
ThunderStorm	Ovesny et al., 2014	N/A
Redundant cross-correlation	Wang et al., 2014	N/A
DBSCAN	This paper	https://doi.org/10.5281/zenodo.7016376
Voronoi Tessellation	This paper	https://doi.org/10.5281/zenodo.7016376
Varicosity segmentation	This paper	https://doi.org/10.5281/zenodo.7016376
Swift	Ulrike Endesfelder Lab, Bonn University	https://swifttracking.slack.com/join/shared_invite/zt-m6e3fb9u-J2lBX3uaHY0v3JZwiOeSw#/shared-invite/email
dSTORM colocalization	This paper	https://doi.org/10.5281/zenodo.7016376